Investigating the Nature of Brine Pockets on Ceres using Hyperspectral mapping

LYNETTE DIAS
July 2022

SUPERVISORS:
Wim Bakker, MSc.
Dr. Frank van Ruitenbeek

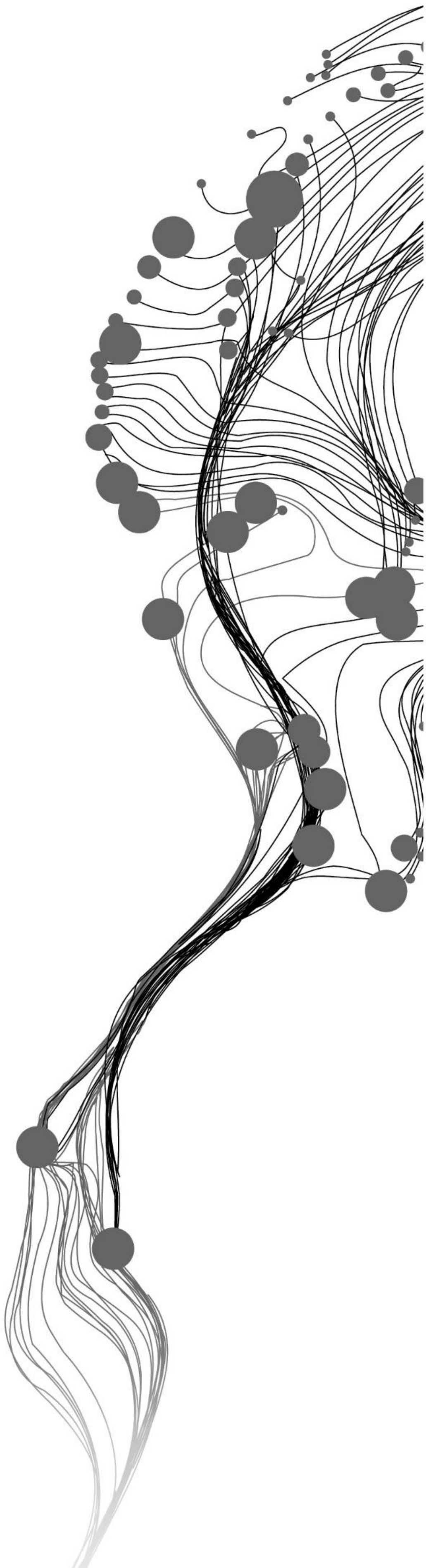

Investigating the Nature of Brine Pockets on Ceres using Hyperspectral mapping

LYNETTE DIAS
Enschede, The Netherlands, July 2022

Thesis submitted to the Faculty of Geo-Information Science and Earth Observation of the University of Twente in partial fulfilment of the requirements for the degree of Master of Science in Geo-information Science and Earth Observation.

Specialization: Applied Remote Sensing for Earth Sciences

SUPERVISORS:
Wim Bakker, MSc.
Dr. Frank van Ruitenbeek

THESIS ASSESSMENT BOARD:
Dr. Chris.A. Hecker (Chair)
Dr. Ottaviano Ruesch (External Examiner, University of Münster)

"Space: the final frontier….to explore strange new worlds. To seek out new life and new civilizations. To boldly go where no one has gone before!"

ABSTRACT

Dwarf planet Ceres happens to possess the extraterrestrial life trifecta- water, organic materials and carbon, and energy making it a prime candidate for astrobiological studies. The most striking feature of this dwarf planet are the bright spots called 'faculae' on its surface formed by the deposition of minerals from briny fluids that erupt from subsurface brine pockets onto the surface and undergo flash freezing. Previous studies used mixtures of spectral endmembers to model the average spectrum of the faculae. This study aimed to investigate the nature of brine pockets on Ceres using hyperspectral datasets collected by the Dawn spacecraft 's VIR instrument.

A preprocessing process was developed to assess the data quality and the extent to which spectral artifacts affected it and to reduce or remove these artifacts. Artifacts like negative pixels, spectral spikes and vertical stripes were seen in the datasets due to sensor defects. An alternative method to the artifact matrix used by the VIR team was employed which removed the negative pixels and spikes and minimized the vertical stripes. The spectral analysis was carried out using summary products and wavelength mapping. The summary products targeted at CO_2 and water ice highlighted regions of interest in the craters. The carbonate products that show Mg/Ca/Fe carbonates also showed regions of interest on the crater floors and crater slopes. The BD2600 product which highlights water vapour showed high values in the center of Occator crater where the faculae are known to be found. The wavelength maps highlighted regions of interest from which spectra were extracted and compared with spectra of Ca/Fe and Mg carbonates as well as dolomite and natrite ($Na_2(CO_3)$) from the RELAB spectral database. They were also compared to spectra from previous studies.

Two prominent wavelengths at which absorption features were seen were 2.7 μm and ~3 μm which were found to be due to NH_4 salts and anhydrous carbonates from previous studies. Absorption features matched the spectrum for carbonates (mainly composed of dolomite) at ~2.7 μm and of natrite at ~3.9 μm. No new minerals were identified, and the absorption features of the spectra of the regions identified showed the similar absorption features of two different carbonates. This led to an inconclusive result of the specific minerals present in the faculae but a definite indication of the presence mineral groups like carbonate and ammonium.

The lack of mineral identification made the study of the chemical conditions in the brine pockets impossible as the association of the minerals was to be used to make this inference.

Keywords: hyperspectral, wavelength mapping, summary products, spectral artifacts

ACKNOWLEDGEMENTS

I would like to thank my supervisors- Wim Bakker and Frank van Ruitenbeek. Their ideas and suggestions were incredibly in sync which made them the perfect team to navigate this tricky path of planetary mapping with. I would also like to thank my chair Chris Hecker for his feedback during my proposal and midterm.

A special thanks goes out to my mentor Harald van der Werff for his advice through the entirety of my Master's and to Bart Krol for lightening the mood before my presentations and making me less nervous to present.

To my friends in room 5-036: Sahara, Diana, Enzo, Biman, Binita, Sachita and Nithesh, thank you for being the wind beneath my wings, for keeping me motivated when things got hard and for keeping me in splits with all your funny anecdotes during the tea breaks and plank sessions.

Mahnoor, Dewi and Arvind, thanks for always being there when I needed advice or a friend to talk to. Lexy, Som and Gech- I'm grateful for your feedback during my proposal and all the group projects we tackled together.

And finally, a big thank you to Mom, Dad and Luke, thanks for believing in me, Always.

TABLE OF CONTENTS

LIST OF FIGURES

LIST OF TABLES

1. INTRODUCTION

Ceres, the first dwarf planet to be discovered in our Solar System, happens to possess the extra-terrestrial life trifecta- water, organic materials and carbon, and energy making it a prime candidate for astrobiological studies (Castillo-Rogez et al., 2021). It was discovered in 1801 by Giuseppe Piazzi (Carry et al., 2008), and its location in the asteroid belt between Mars and Jupiter at a distance of 2.767 AU from the Sun led to it initially being classified as an asteroid (Williams et al., 2018) but later re-classified as a dwarf planet because of its size (Pilcher, 1989).

The surface of Ceres as studied from Hubble Space Telescope images (Thomas et al., 2005) showed a dark uniform albedo surface with a few high albedo bright spots. These bright spots were found to be mineral deposits, and were called 'faculae' (Stein et al., 2019). The nature of these deposits forms the basis of my research.

1.1. Background

The interest in Ceres led to a mission to the asteroid belt that led to a more detailed study of the faculae and the surface of Ceres-the Dawn Mission. The Dawn spacecraft's payload and the studies carried out on the faculae will be introduced in this section.

1.1.1. The Dawn spacecraft

On March 6th, 2015, NASA's Dawn spacecraft reached Ceres, after investigating asteroid Vesta, and became the first spacecraft to orbit a Dwarf planet (Russell et al., 2016). The spacecraft was equipped with three instruments: The Framing Camera (FC), the Visible and InfraRed mapping Spectrometer (VIR), and the Gamma Ray and Neutron Detector (GRaND) (Williams et al., 2018).

The VIR spectrometer was contributed by the Istituto Nazionale di Astrofisica (Italian National Institute of Astrophysics- INAF) with support from the Agenzia Spaziale Italiana (Italian Space Agency-ASI); it is a hyperspectral spectrometer that covers the visible wavelengths between 0.25-1.05 μm- the VIS channel, and the infrared wavelengths between 1-5.1 μm, the IR channel (De Sanctis et al., 2012). It was designed to meet the Dawn Mission's objective of determining the minerals present on the surface of Ceres in their geologic context (De Sanctis et al., 2012).

The Framing Camera was contributed by the Max Planck Institute for Solar System Research and the Deutsches Zentrum für Luft- und Raumfahrt (German Aerospace Center- DLR). It was designed to gather information on the shape, topography and geomorphology of the surface of Ceres and complement the information obtained from the other instruments (Sierks et al., 2011). The first study using Dawn's Visible and InfraRed mapping Spectrometer (VIR) data was conducted by De Sanctis et al., (2015), who created a spectral model for the average Ceres spectrum by taking the median of ~2500 spectra obtained during the initial orbital phases and comparing this to spectra from mineral mixtures in the laboratory. The spatial resolution of the datasets used ranged from ~1.3km to 410m. The Occator crater faculae composition was modelled using this average spectrum as a starting point and found sodium carbonates, phyllosilicates, ammonium carbonates and ammonium chloride (De Sanctis et al., 2016).

1.1.2. Studies on the Faculae

Studies on the possible modes of formation of the faculae showed that they were associated with impact craters and predominantly form in crater floors, crater rims or walls and crater ejecta (Stein et al., 2019). The floor faculae were theorized to have formed by the upwelling of substances rich in volatiles that are generated by impact induced heating or by the impact induced upwelling of subsurface brines. The brines then underwent flash freezing- a process known as cryovolcanism, and subsequently deposited the minerals (Ruesch et al., 2019).

The mean density of Ceres calculated from NASA's Dawn spacecraft data was 2162 ± 8 kg m^{-3} (Park et al., 2016) implying that Ceres' interior was composed of a small solid core, a liquid mantle and a water ice-rich crust (Bland et al., 2016; Marchi et al., 2016). Thus, heat generated by an impact could generate brine pockets, and fractures resulting from the impact could always provide fluid pathways to the surface (De Sanctis et al., 2019; Stein et al., 2019)

This mode of formation for the faculae was also supported by simulations created on the formation of Occator crater which show a large volume of subsurface material heated enough for water ice to melt and form hydrothermal fluids (Bowling et al., 2019). Figure 2 shows two simulated cases, 2A shows the subsurface temperature immediately after the impact, with temperatures high enough to support liquid water and 2B shows the same region 100 kyr after the impact when the temperatures have dropped below the melting point of water at the surface of the crater implying that no fresh deposits could form.

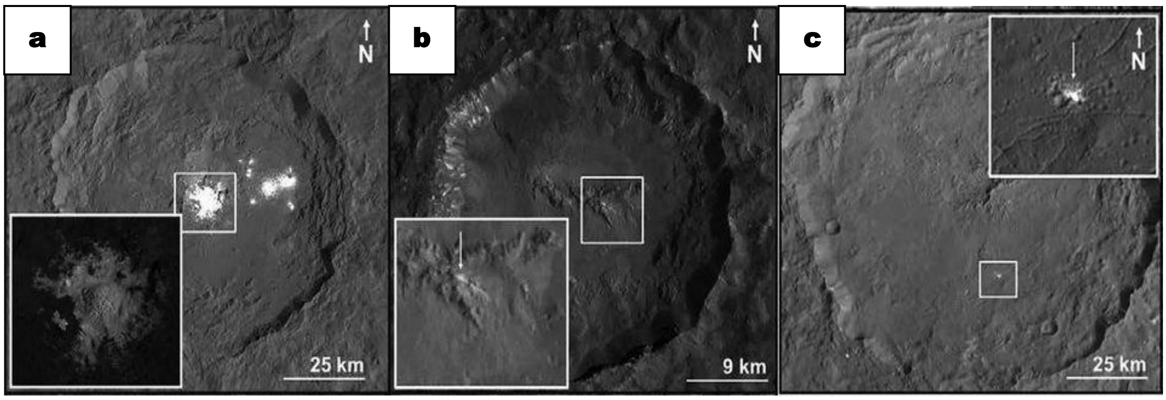

Figure 1: Images of faculae on Ceres taken by the Dawn Framing Camera. a) Occator, b) Haulani and c) Dantu crater (Stein et al., 2019)

Scully et al. (2020) built upon this simulated model and made use of ~10m/pixel XM2 clear filter mosaic images (Figure 1) to observe the morphology of the faculae in Occator crater which they found to be similar to hydrothermal deposits on Earth and they concluded that the faculae deposits were formed from the hydrothermal brines. The possibility of brines still being present is supported by gravity measurements made by NASA's Dawn spacecraft that showed mass heterogeneities under Occator which are believed to be brine concentrations (McCord et al., 2021).

Floor faculae have been observed in 8 craters on Ceres and range in area from <1 km^2 to >120km^2 (Stein et al., 2019) with some craters having more than 1 facula like the Cerealia, Vinalia and Pasola facula in the Occator crater.

Organic compounds were found in the faculae at Ernutet crater mixed with other minerals indicating that they probably deposited from the same source (De Sanctis et al., 2019). The spectral modelling of the Ernutet region showed that kerite had the best fit in terms of the shape of the absorption feature at 3.4 μm (Moroz et al., 1998; Raponi et al., 2019). De Sanctis et al., (2020) detected hydrated sodium chloride- hydrohalite in the brine deposits at Occator crater. This discovery is of great significance because hydrated sodium chloride is unstable at Ceres' surface environment and would have dehydrated in ~100 years into halite which does not have any spectral features in the VIR wavelength range (De Sanctis et al., 2020). This indicates that

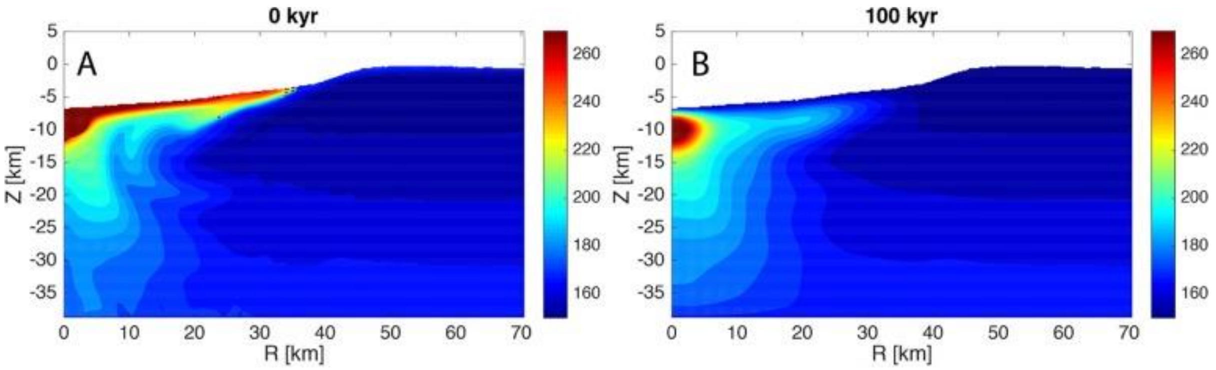

Figure 2: Simulation of an Occator like crater showing the temperature of heated material below and on the crater floor at the time of impact (A) and 100 kyr after the crater formed (B) after the crater floor temperatures fall below the melting point of ice (273K seen as a deep red colour) and/or the eutectic point of the brine (figure taken from Bowling et al., 2019). The colour scale shows the temperature in Kelvin.

the brine deposits have some source of hydration and that this brine emplacement is recent or even still occurring today.

Studies investigating subsurface conditions using elements and minerals detected on the surface have been carried out on other planets like the evaporite deposits of the Terra Meridiani on Mars which are proposed to be formed from groundwater upwelling onto the surface, where estimates were made of the groundwater ph and redox conditions (Baldridge et al., 2009). However, the surface temperatures and crustal mineralogy of Mars is very different from Ceres, which bears more resemblance to some icy bodies in the Solar System. Studies modelling the effects of cryovolcanic chemical compounds detected on the surface on subsurface conditions of other icy worlds such as on Europa and Enceladus (Manga and Wang, 2007) and Pluto (Martin and Binzel, 2021) have been carried out however, they involve modelling pressure gradients which is beyond the scope of this study. Such studies have not been carried out on Ceres yet.

A detailed analysis of the faculae minerals in craters on Ceres without the use of any predefined spectral endmember to investigate the chemical conditions in the brine pockets has not been carried out on Ceres and that is the research gap that this study aims to fill.

1.2. Research problem

The research problem this study addresses is finding a method to investigate the chemical conditions in crater subsurface brine pockets by mapping crater faculae mineralogy using methods that do not involve the use of predefined spectral endmembers.

The surface mineralogy of the Occator crater, has been modelled before using Hapke's radiative transfer model (De Sanctis et al., 2020; Raponi et al., 2019), however this model requires the input of spectral endmembers which this study aims to eliminate. This study investigates the mineralogy of three craters- the Occator, Dantu and Haulani and will also create a spectral library for the faculae minerals identified.

1.3. Research objectives

The primary objective of this study is to investigate the chemical constraints set by brine deposit mineralogy on the chemical conditions present in the brine pockets below craters on Ceres. The sub-objectives to achieve this are as follows:

1. To assess the quality of the VIR datasets and develop a preprocessing pipeline to remove or reduce spectral artifacts.
2. To identify the minerals deposited by brines in crater faculae from their spectral signatures.
3. To create a spectral library of the minerals identified and incorporate the minerals detected by previous studies of the Occator crater as well.
4. To map the minerals in the brine deposits.
5. To study the geological context of the mapped minerals on the crater floor.
6. To compare the brine deposit mineralogy of the Occator, Haulani and Dantu craters.

1.4. Research questions

1. What does the presence of the identified minerals tell us about the chemical conditions prevalent in the brine pockets?
2. What are the wavelengths at which common mineral groups occur at and are there any spectral artifacts/noise in these regions within the datasets?
3. Will the proposed preprocessing methods this study uses affect any of the spectral signatures present by removing bands in which features of previously identified minerals occur?
4. How are the mineral deposits spatially associated with the crater geology?

5. Does the similarity/dissimilarity of crater faculae mineralogy of the three craters imply a possible common brine source?

1.5. Study area

This study will focus on crater floor faculae in three impact craters on Ceres- Occator, Dantu and Haulani. The locations of the three craters are shown in Figure 3. All three craters are relatively recent (Mest et al., 2021; Stein et al., 2019) and hence their faculae deposits would not show pronounced alterations due to space weathering. Weathered products would hinder the primary objective of this study which is to investigate the nature of the subsurface brines. Dehydrated halite deposits will not be detectable as well due to lack of absorption features in the VIR data range. Occator crater also happens to have two of the biggest faculae on Ceres, the Cerealia and Vinalia faculae (Raponi et al., 2019).

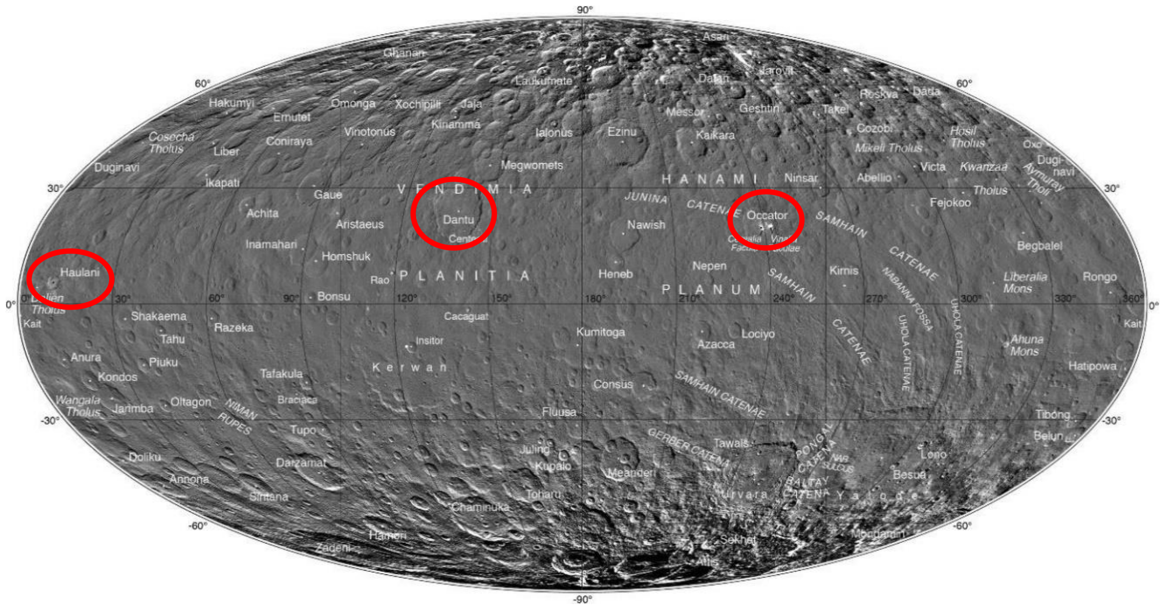

Figure 3: Map of Ceres showing the locations of the three craters to be studied-Occator, Dantu and Haulani modified from De Sanctis et al., (2020)

1.6. Dataset

The datasets used in this study are from the VIR spectrometer on NASA's Dawn spacecraft. The spatial resolution of the datasets depends on the altitude of the spacecraft: the Survey phase at an altitude of ~4400 km, the High Altitude Mapping Orbit (HAMO) at ~1500km and the Low Altitude Mapping Phase (LAMO) ~378 km. The VIR had a spatial resolution of 100m/pixel during the LAMO phase. During the last phase of its mission- the second extended mission (XM2) phase, Dawn imaged Occator crater at a higher resolution with an altitude of ~35km. The VIR data products are stored as data cubes in the Planetary Data System (PDS) archive as Level 1B products for each orbit phase.

The VIR instrument has datasets for the Visible and Infrared range of the electromagnetic spectrum; however, this study will not utilize the visible wavelength range. Any mention of the VIR dataset henceforth only refers to the infrared part of the spectrum.

The imaging spectrometer used by Dawn is a push-broom scanner which records data in the form of a hyperspectral 'cube' with two spatial and one spectral dimension (Figure 4). The signal is stored as raw digital numbers (DNs).

NASA used a planetographic coordinate system to map Ceres which consists of positive east longitudes over a spherical reference surface with the prime meridian passing through the Kait crater (Raymond, C. A., Roatsch, 2015). The tiling scheme used by the Dawn mission team is the one suggested by Greeley and Batson (1990) for medium-sized planetary bodies, wherein the body is divided into 15 map quadrangles- 5 equatorial quadrangles in the Mercator projection, 4 northern and 4 southern quadrangles in the Lambert projection and 2 at the poles in stereographic projection.

The Dawn Framing Camera images were used as a base layer for the wavelength mapped images to provide a spatial context for the identified minerals. FC imagery has a low spectral resolution of ~40nm but its spatial resolution at the LAMO phase is 60m/pixel. The FC resolution for Occator crater in the XM2 phase was ~3m/pixel, however, this dataset was only available for Occator crater.

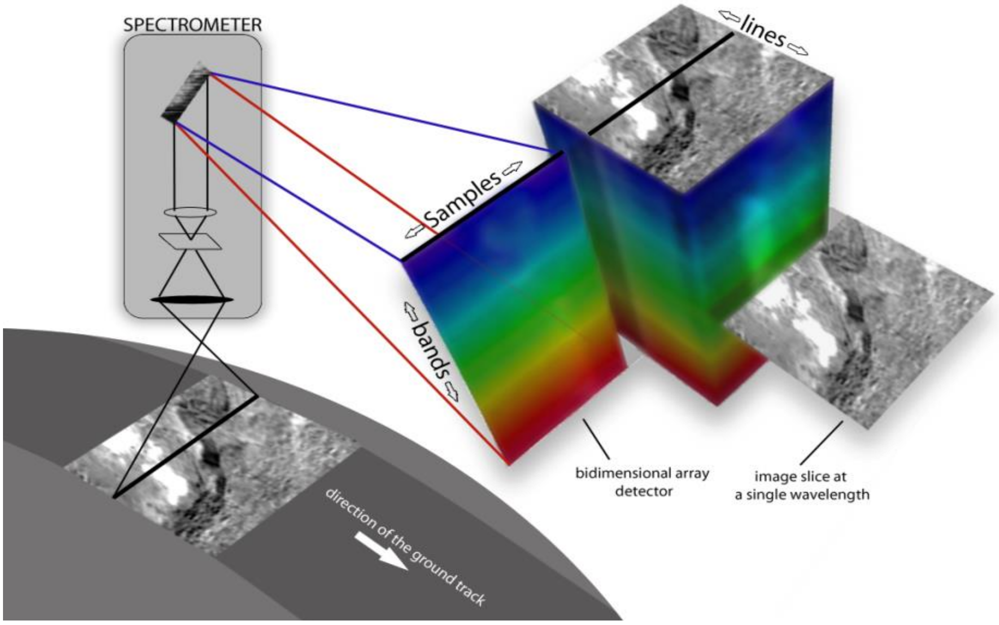

Figure 4: Image adapted from Carozzo et al. (2016)

2. METHODOLOGY

To investigate the nature of the brine deposits, the datasets had to be downloaded, preprocessed and corrected before they could be used for spectral analyses to answer the proposed research questions. The methodology used in this study involves the following parts- the data download, solar correction, data quality assessment, artifact removal, the creation of the wavelength maps and summary products and the integration of the wavelength maps with the framing camera images. The steps used will be defined in this chapter. The software used to process the data are as follows:

1. Hyperspectral Python (HypPy)
2. Integrated Software for Imagers and Spectrometers (ISIS3)
3. ENVI
4. IDL Workspace

2.1. VIR Data download and Preprocessing

This study uses datasets from the VIR instrument. This subsection explains the preprocessing steps used for the VIR data. Figure 5 provides an overview of the entire process.

The VIR instrument datacubes were downloaded from NASA's Planetary Data System (PDS) archive. Two levels of calibration are available for download- Level 1A and Level 1B. The Level 1A (EDR) data comprise the raw datacubes stored as digital numbers. They are then radiometrically calibrated to give the Level 1B (RDR) datacubes which were used in this study[1]. This calibration converts the data from digital numbers to spectral radiance ($Wm^{-2}\ sr^{-1}\ \mu m^{-1}$).

The datasets are listed with the product number under the orbit phase and cycle they were obtained in. The geometric data for each dataset including the ground coordinates for each datacube can be found in the INDEX table which was used to select the files with imagery for the selected craters. Each dataset had 6 files as shown in table 1.

Table 1: The VIR dataset file structure

File	File type
Datacube label	.LBL
Datacube	.QUB
Housekeeping file table	HK.TAB
Housekeeping file label	HK.LBL
Quality label	QQ.LBL
Quality cube	QQ.QUB

[1] The calibration procedure from EDR to RDR data can be found on the PDS archive in the VIR_CALIBRATION document within the CALIB folder available for each dataset.

The datacube can only be opened in HypPy or ENVI after the creation of a header file from the information stored in the label file. This step was done in IDL Workspace using code provided in the PDS archive. This step can also be carried out in ENVI by entering the same information, however this involves many steps and can easily lead to errors if the data is entered incorrectly.

The preprocessing steps were adapted from the process outlined by the VIR spectrometer team for the Dawn Mission (Carrozzo et al., 2016; Rousseau et al., 2019). Firstly, a solar correction was applied to the Level 1B dataset. Following this a ground correction step was applied.

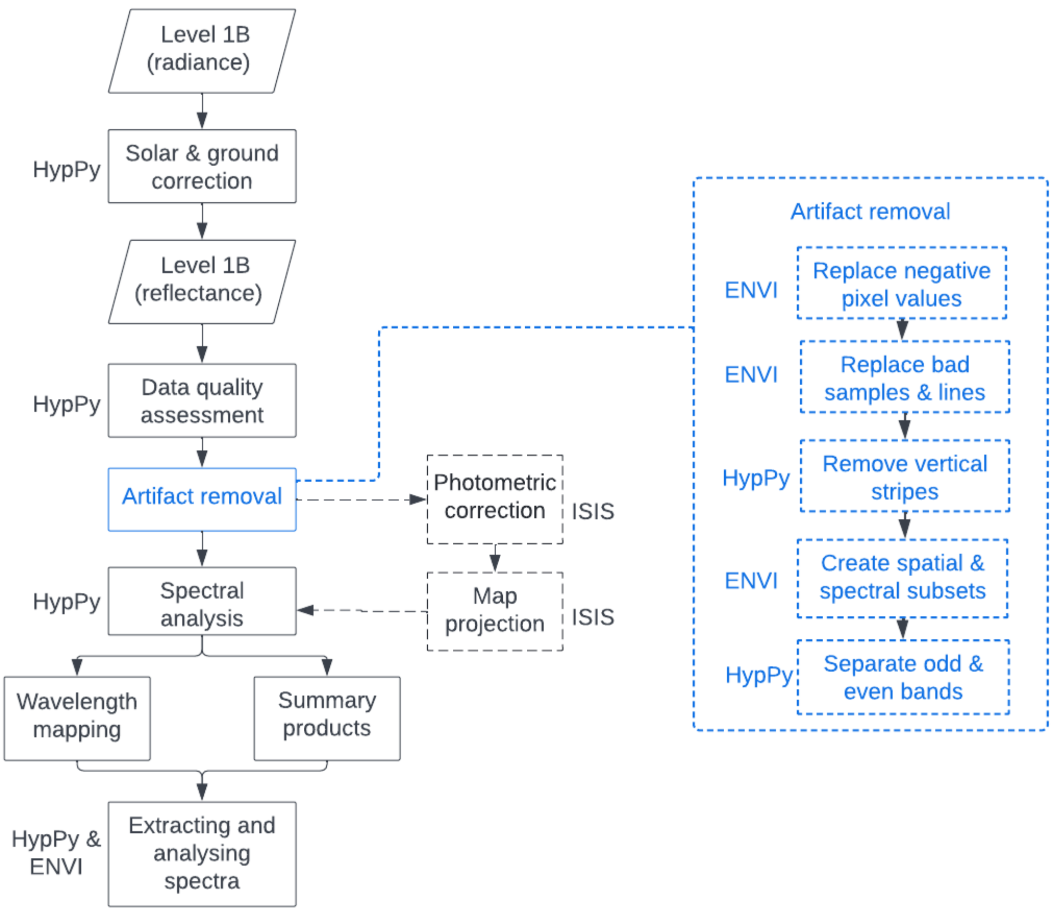

Figure 5: The processing steps followed in this study. The dashed black boxes indicate steps that could not be carried out in the sequence but were executed separately in ISIS. The dashed blue box elaborates the steps used in the artifact removal procedure

2.1.1. Solar correction

To convert the information in the Level 1B datacubes from radiance to calibrated radiance factor (I/F), which is the reflectance, the spectra need to be divided by the solar spectrum. The Solar correction was carried out in HypPy. The solar spectrum used was obtained from the PDS archive and the procedure was carried out in HypPy. The tool used in Hyppy does not take the heliocentric distance into account and hence an additional calculation had to be applied. The overall equation used for the solar correction was:

$$I/F = (S/S_i)*\pi*(ssd/K)^2$$

S is the calibrated radiance measured by the VIR instrument in $Wm^{-2}\ \mu m^{-1}sr^{-1}$. S_i is the solar irradiance for the VIS and IR channels, and ssd is the spacecraft solar distance (heliocentric distance) in km and K is the distance of 1 AU in km.

2.1.2. Ground correction

To correct for a positive slope that can be seen in the VIR spectra in the VIS-NIR region when compared to spectra obtained from ground based measurements on Earth (Carrozzo et al., 2016), a ground correction factor was applied. The ground correction factor was available in the PDS archive and is the ratio of the spectrum of Ceres measured from Earth to the VIR spectrum measured by Dawn, where both spectra are normalized at 0.550 µm. Carrozzo et al., (2016) stated the lack of understanding on the origin of the positive slope at the time of publication of the paper, however more recent studies have also incorporated this step (Rousseau et al., 2019). The VIR spectra were multiplied by the ground correction factor using the spectral math tool in HypPy. The equation used is provided in annex 1.

2.2. Data Quality Assessment

The VIR dataset also contained spectral artifacts that needed to be removed before spectral information could be extracted from the data else, they could lead to erroneous interpretations of minerals and surface features. The artifacts had to be identified and then removed and the correct identification of them was necessary to prevent the distortion of an absorption feature due to incorrect artifact removal. The artifacts present in the data were identified during the data quality assessment stage.

The spectra are affected by three types of artifacts in the instrument response function, which are distinctly seen when the datacube is displayed in HypPy. Vertical stripes, spectral spikes and the odd-even band effect are the most striking artifacts.

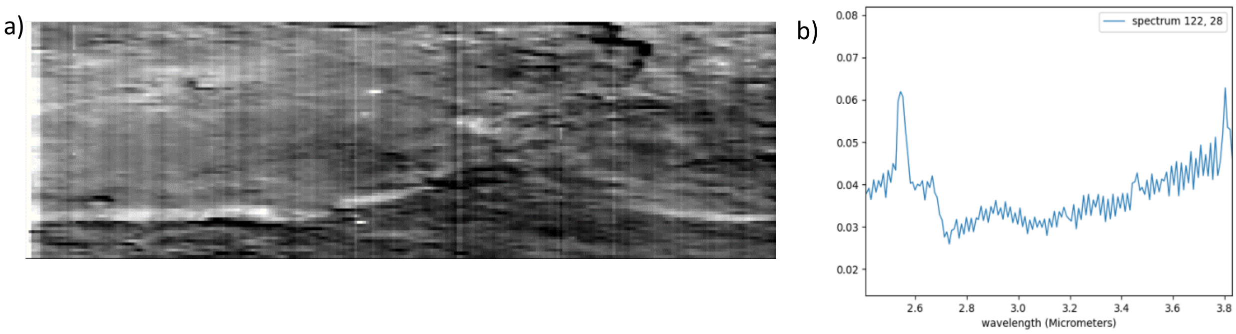

Figure 6: a) The image shows Band 104 of VIR_IR_1B_1_494523791_1. Vertical stripes (columns) can be seen across the image. b) The odd even effect producing a jagged spectrum.

Vertical stripes

If single bands are viewed at a time, vertical stripes are seen across multiple bands in the same image columns/samples (Figure 6). This occurred due to an issue with the charged couple device (CCD) that stores measured radiance values (Carrozzo et al., 2016). Not all neighbouring CCD elements have the same sensitivity and instrument response resulting in clearly visible stripes between image columns (Gómez-Chova et al., 2008). The slit width of the instrument also varies with temperature and may affect the response as noted by Rousseau et al., (2019).

Odd-even band effect

The spectra show a jagged pattern called the odd-even band (wavelength) effect due to the electronic offset of the signal detectors(Gómez-Chova et al., 2008). Radiance information is collected by the CCD array coupled to multiplexers which read the odd and even signal of the detector rows ie. the odd and even bands. The difference in the electronic offset between the odd and even bands results in the jagged effect of the spectra (Carrozzo et al., 2016).

Spectral spikes

An analysis of the image statistics was done in ENVI and the presence of many outliers was seen, as well as the presence of negative value pixels. The spikes are caused by detector pixels being affected by random anomalies like cosmic rays striking the detector (Carrozzo et al., 2016).

2.3. Artifact Removal

The artifacts identified then had to be removed before the spectra could be analysed. This study was undertaken primarily to identify minerals and hence the bands in which mineral signatures were present-as identified in previous studies had to be preserved and not modified to the extent where absorption features got affected. The elemental groups identified include carbonates, ammonium, and hydroxyl.

2.3.1. Replacing negative pixel values

The spectral math tool in HypPy was used to replace negative pixel values using the equation

$$((S1< 0)* (-999)) + ((S1> 0)* S1)$$

This identified negative values and replaced them with -999 and identified positive values and replaced them with their original values leading to a datacube where all the negative pixels were replaced. A mask of the negative pixels was also created to identify their location in the cube easily. This mask also highlighted bad samples and lines which were then replaced or removed. Certain regions in the image had a cluster of bad pixels that could not be replaced or removed and these bands had to be removed during spectral subsetting later.

2.3.2. Replacing bad samples and lines

For bands with only a single bad sample, the spatial pixel editor tool in ENVI was used to replace the bad sample with an average of its two neighbouring samples. Bands with many bad samples and more than two adjacent bad samples were removed. A bad line (line 112 in VIR_IR_1B_1_493567338_1) seen across multiple bands was removed using the remove bad lines tool in ENVI. This tool removed the bad line in all bands.

2.3.3. Removing Vertical stripes

Vertical stripes were reduced by means of the destriping filter tool in HypPy. This filter compares the statistics-the mean and standard deviation, of a chip cell with cells in its 3x3 neighbourhood across the entire y direction of the datacube. Pixels that have values above thresholds set by the user are replaced by an average of their neighbouring pixels. The tool also provided a list of bad pixels.

2.3.4. Spatial and Spectral subsetting

Bad bands were removed by spectral subsetting and the first few samples of the image were removed by spatial subsetting. The number of bands, samples and lines removed differs from dataset to dataset.

2.3.5. Separating odd and even bands

A spectral subset was created to separate the odd and even bands to eliminate this effect and result in a smoother spectrum. This step was used in lieu of calculating a weighted average of the band and its two adjacent bands that was applied in the artifact matrix proposed by Carrozzo et al., (2016). The spectral subsets were created using the Resize Data (Spatial/Spectral) tool in ENVI by manually selecting the odd bands and saving it as a separate .QUB file and doing the same for the even bands.

2.4. Spectral Analysis

The distinct spectral signatures of mineral groups can be used to identify, map and analyze their spatial associations in an image using techniques like summary products and wavelength mapping Neither method requires the input of mineral endmembers and their spectra which is why they were chosen for this study to investigate the minerals present on the surface. The minerals identified and their association with each other on the surface will then be used to compare the mineralogy of the three craters and formulate an understanding of the subsurface.

2.4.1. Summary Products

A summary product is a parameter that targets a specific spectral feature indicative of a certain mineralogy, and extracts it using an algorithm involving combinations of bands from the dataset (Pelkey et al., 2007). The resulting product shows the variations of this spectral feature across the image. The Pelkey summary products were made for the CRISM dataset based on information obtained about the surface mineralogy of Mars from OMEGA data. Viviano-Beck et al., (2014) improved on the original products using the detailed mineralogical information provided by the CRISM dataset. The Viviano-Beck products were used in this study as they were designed to represent mineral diversity on the surface more so than the Pelkey products which would be beneficial in a study focused on investigating mineral deposits. Although the products were designed to study the Martian surface, they utilize bands that are present in the VIR dataset which is why they can be applied in this study as well.

The creation of the summary products was carried out in HypPy. They utilise wavelengths from 0.77 μm to 3.92 μm, hence the dataset was used in its entirety before spectral subsetting. The odd-even effect was not an issue because the products used mathematical operations on single bands.

2.4.2. Wavelength Mapping

Wavelength Mapping is a method developed by Van Ruitenbeek et al., (2014) which finds the wavelength and depth of the deepest absorption feature in the spectra of a hyperspectral cube within the wavelength range set by the user. It is a two-step process that results in a 'wavelength map' which uses a colour legend to indicate the wavelength position and depth of the deepest absorption feature in the mapped image. This method has been successfully employed in the exploratory analysis of mineral deposits on Mars and produces wavelength position maps that show the spatial diversity of minerals on the surface without the need of predefined endmembers (Van Ruitenbeek et al., 2014). This is why it was chosen for this study. This step was carried out in HypPy.

2.5. Photometric correction and Map projection

This process was carried out in Integrated Software for Imagers and Spectrometers (ISIS) a software developed for planetary mapping of NASA imagery created by USGS (Sides et al., 2017). This software only runs on Linux although it can be operated on Windows using a Windows Subsystem for Linux (WSL). ISIS cannot modify PDS datacubes in the .QUB format and these have to be converted to ISIS cubes in the .cub format using the *dawnvir2isis* tool. This conversion requires the input of the datacube, its label, the housekeeping cube and its label.

The navigation and ancillary data available in the form of SPICE[2] kernels are needed for the photometric correction and map projection steps. They can be downloaded or accessed through the ISIS SPICE web service, although several errors occur while using the web service and hence the entire Dawn Mission SPICE kernels were downloaded. The SPICE data was then added to the cube using the spiceinit tool. The map projection was carried out using the cam2map tool. A mosaic of the FC images was created using the qmos tool.

[2] SPICE- **S**pacecraft ephemeris, **P**lanet ephimerides, **I**nstrument information, **C**amera matrix, **E**vents information

3. RESULTS

As explained in the previous chapter, the first steps of the data processing involved the solar and ground correction. This was then followed by the data quality assessment and the artifact removal. The spectral analysis of the preprocessed datasets was carried out by creating summary products and using wavelength maps.

VIR datacubes for each crater were selected. For Occator and Haulani crater only one datacube was selected each. Dantu crater has a much larger diameter and hence 3 images were selected to cover its extent. The datasets selected capture the entire crater and some parts of the craters' surroundings as well.

Table 2: VIR datasets selected for this study

Crater	VIR datacube	bands	samples	lines
Occator	VIR_IR_1B_1_493567338_1	432	256	128
Haulani	VIR_IR_1B_1_494731110_1	432	256	76
Dantu	VIR_IR_1B_1_494523791_1	432	256	76
	VIR_IR_1B_1_495408230_1	432	256	76
	VIR_IR_1B_1_495474811_1	432	256	76

3.1. Solar and Ground correction

The results of the solar correction that resulted in the conversion of radiance values to reflectance can be seen in figure 7 which shows the changes in the spectra of the same pixel (103,51). The curve goes up after 3.5 µm because of thermal emissions from the surface of Ceres. Figure 8a shows the spectra of the same pixel before and after the ground correction factor was applied. The changes are mainly seen in the region from 1-2.25 µm (figure 8b).

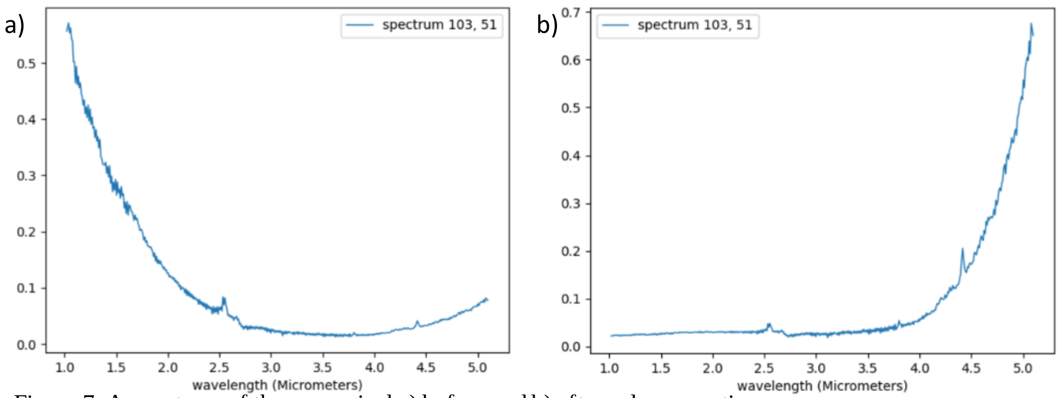

Figure 7: A spectrum of the same pixel a) before and b) after solar correction

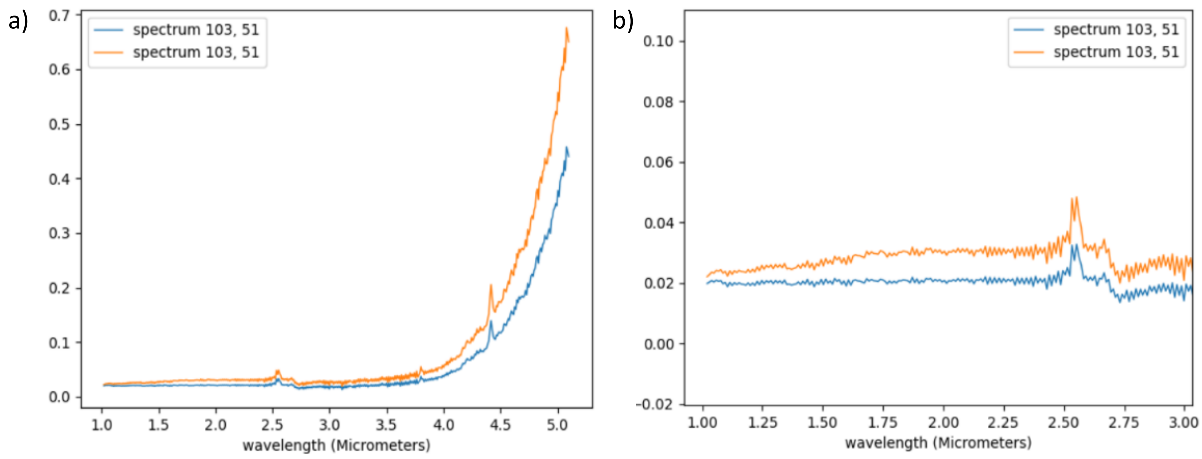

Figure 8: a) A spectrum of the same pixel before and after the ground correction factor was applied. b) The change to the spectrum can be seen clearly in the wavelength range 1-2.25 μm

3.2. Data quality assessment

The data quality assessment carried out before spectral analysis showed the presence of many spectral artifacts, seen in all of the datacubes. The artifacts observed were vertical stripes in the spatial domain and spikes and odd-even band effect in the spectral domain. The band statistics were computed-mean and standard deviation, that show the effect of the bad pixels on the statistics and also provide insights on the samples and bands in which these pixels occur.

The bad pixels and bad samples (columns) can be seen in band 1 of VIR_IR_1B_1_493567338_1 in figure 9. The figure also shows the resulting spectrum from a bad pixel and the highly negative reflectance values can be seen in this spectrum.

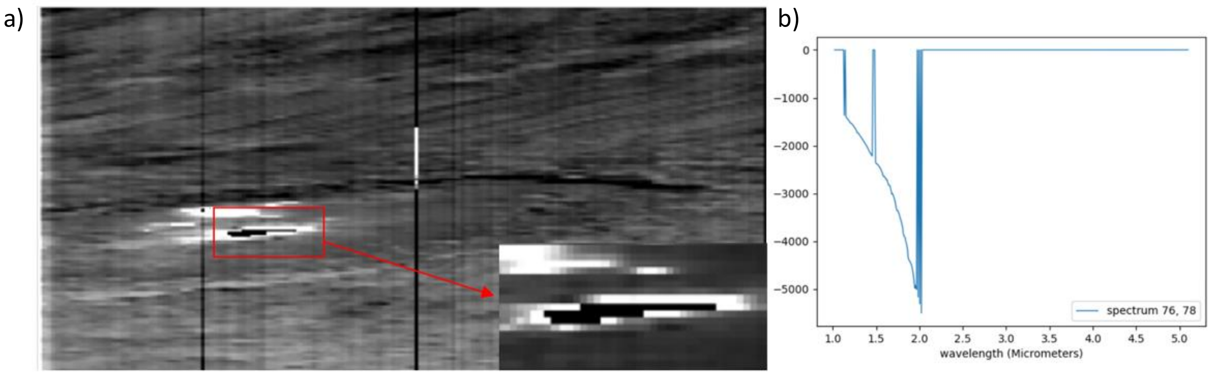

Figure 9: The central part of Occator crater shows a cluster of bad pixels which can be seen clearly in the enlarged box. A spectrum of one of these pixels can be seen on the graph on the left.

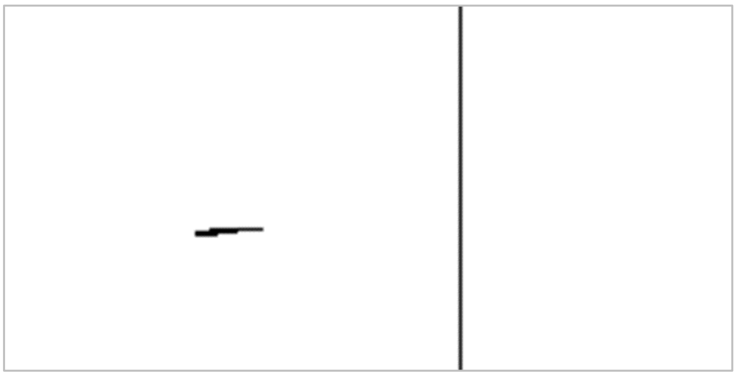

Figure 10: Mask band showing a cluster of bad pixels and a bad sample

3.3. Artifact removal

The bad pixels were removed first by converting all negative valued pixels to -999. A mask was created to highlight the negative pixels as well which is seen in figure 10 that shows a mask for band 1 of VIR_IR_1B_1_493567338_1. A cluster of pixels with negative values is distinctly visible along with a bad sample. The mask made it easier to locate bad pixels, samples and lines.

The process to correct these artifacts was carried out in ENVI using the spatial pixel editor. Bad pixels were replaced with an average of the neighbouring 8 pixels. A bad line was only seen in VIR_IR_1B_1_493567338_1 of the Occator crater and was removed. None of the other datasets had a bad line. In the case of bad samples, the entire sample (column) was replaced with an average of the two adjacent samples. In some cases, a single pixel in a sample showed negative values but the entire sample showed values lower than its adjacent samples. In these situations, the entire sample was replaced as well.

If a cluster of bad pixels was noted, the band was flagged as bad and removed in the spectral subsetting stage as most of the methods to replace these pixel values involved an average of the surrounding 4 or 8 pixels that would not work in such cases. This was observed in bands 3-126 (1.04-2.203 μm) of VIR_IR_1B_1_493567338_1. This cluster (Figure 9a and 10) was in the middle of the Occator crater in a region of pixels having very high reflectance values in multiple bands as compared to the surrounding pixels in the crater and the outside it.

The Dawn VIR team has provided a list of bands affected by filter boundary positions (Carrozzo et al., 2016) and bad pixel locations in the VIR_CALIBRATION file in the DOCUMENTS folder for each survey phase. The bands were added to the bad bands list and removed during the spectral subsetting later on. The list of pixels flagged as bad for exceeding the destriping filters' thresholds did not match the bad pixels list in the VIR_CALIBRATION document. The bad samples, bands and lines have been listed in table 3.

The results of the destriping filter section 2.3.3 being applied on a datacube that has been spatially and spectrally subsetted can be seen in figure 11. It shows band 213 of datacube VIR_IR_1B_1_494731110_1. The second image is part of a subsetted datacube from which the bad pixel values have been removed and the bad samples have been replaced. The first 8 samples at the left edge of the datacube were removed because their values were much lower than the samples in the rest of the image and were most likely the result of an instrumental error.

The odd-even band effect was tackled by separating the odd and even bands by spectral subsetting. The even bands were chosen for datacube VIR_IR_1B_1_494731110_1 as the odd bands were affected by vertical striping to a greater extent (figure 12). The spectra before and after this step shows how the jagged nature of the spectrum is subdued.

This concluded the preprocessing and artifact removal procedures. Some striping still persists, as well as multiple adjacent samples showing values higher or lower than the surrounding samples. This cannot be attributed to spectral features and is due to sensor errors due to the effect being seen across entire samples. There were no tools for removing samples without splitting the image into two and hence they were left as is.

Table 3: Bad samples, bands and lines in the hyperspectral cubes used

Dataset		Bad band/sample/line numbers
Occator		
VIR_IR_1B_1_493567338_1	Bad bands	1-125, 223-225, all after 370(4.5µm)
	Bad samples	1-5
	Bad lines	112
Dantu		
VIR_IR_1B_1_494523791_1	Bad bands	1-30, 223-226, 342-346, all after 370 (4.5µm)
	Bad samples	1-5
	Bad lines	None
VIR_IR_1B_1_495408230_1	Bad bands	1-18, 24-29, 55-69, 187-194, 223-225, 341-346, all after 370 (4.5µm)
	Bad samples	1-8
	Bad lines	None
VIR_IR_1B_1_495474811_1	Bad bands	1-30, 55-69, 162, 213, 223-225, 341-346, all after 370 (4.5µm)
	Bad samples	1-8
	Bad lines	None
Haulani		
VIR_IR_1B_1_494731110_1	Bad bands	1-20, 55-69, 223-226, 342-346, all after 390 (4.7 µm)
	Bad samples	1-12
	Bad lines	None
Common	Bad bands	49-54, 156-161, 290-293, 357-360

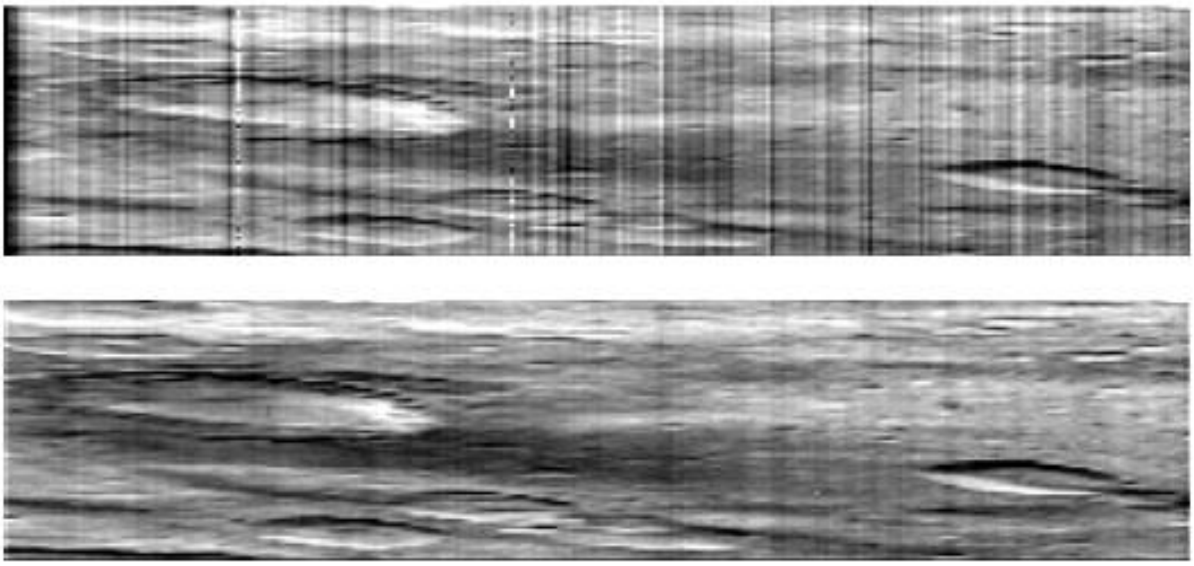

Figure 11: a) Before and b) after the destriping filter was used

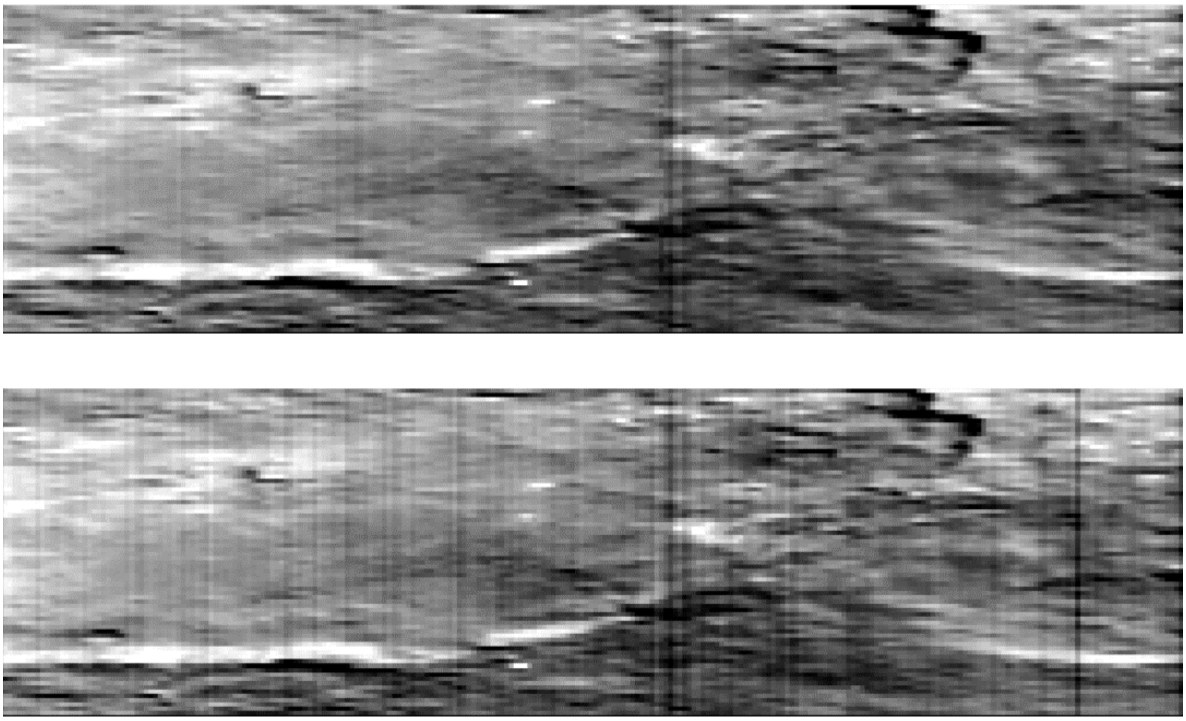

Figure 12: Difference between an adjacent odd and even band that persists even after the destriping filter was used. The odd band (a) shows fewer vertical stripes as compared to the even band (b)

3.4. Spectral Analysis

The results of the two spectral analysis steps-the summary product creation and the wavelength mapping are shown in this section.

3.4.1. Summary Products

The tool used to create the summary products in HypPy calculates all the products and the output is a file with all the summary products as bands. Since the first 20 bands of almost all the datasets were removed, ten of the summary products could not be created. The summary products that highlighted certain features in the datasets can be seen in table 4.

Table 4: Summary products used and their description

Product	Parameter	Rationale
BD1500_2	1.5 µm H_2O ice band depth	H_2O ice on surface or in atmosphere
ICER2	2.7 µm CO_2 ice band	CO_2 versus water ice/soil; CO_2 will be >>1, water ice and soil will be ~1
MIN2295_2480	Mg Carbonate overtone band depth and metal-OH band	Mg carbonates; both overtones must be present
MIN2345_2537	Ca/Fe Carbonate overtone band depth and metal-OH band	Ca/Fe carbonates; both overtones must be present
BD3100	3.1 µm H_2O ice band depth	H_2O ice
BD3400_2	3.4 µm carbonate band depth	Carbonates
CINDEX2	Inverse lever rule to detect convexity at 3.6 µm due to 3.4 µm and 3.9 µm absorptions	Carbonates> 'background' values> 0
BD2600	2.6 µm H_2O band depth	H_2O vapor (accounts for spectral slope)

The following figures show the summary products for the three VIR datasets for Dantu crater, followed by the Haulani crater and the Occator crater. The products have been displayed with a 1%-99% contrast stretch and a green-red colour scale where green indicates low and red indicates high values for that product. The products for the craters have been displayed in a single column to make the positions of erroneous features highlighted by the products due to residual striping clear. The number of samples retained after the spatial subsets were created was not the same which is why the images do not align perfectly.

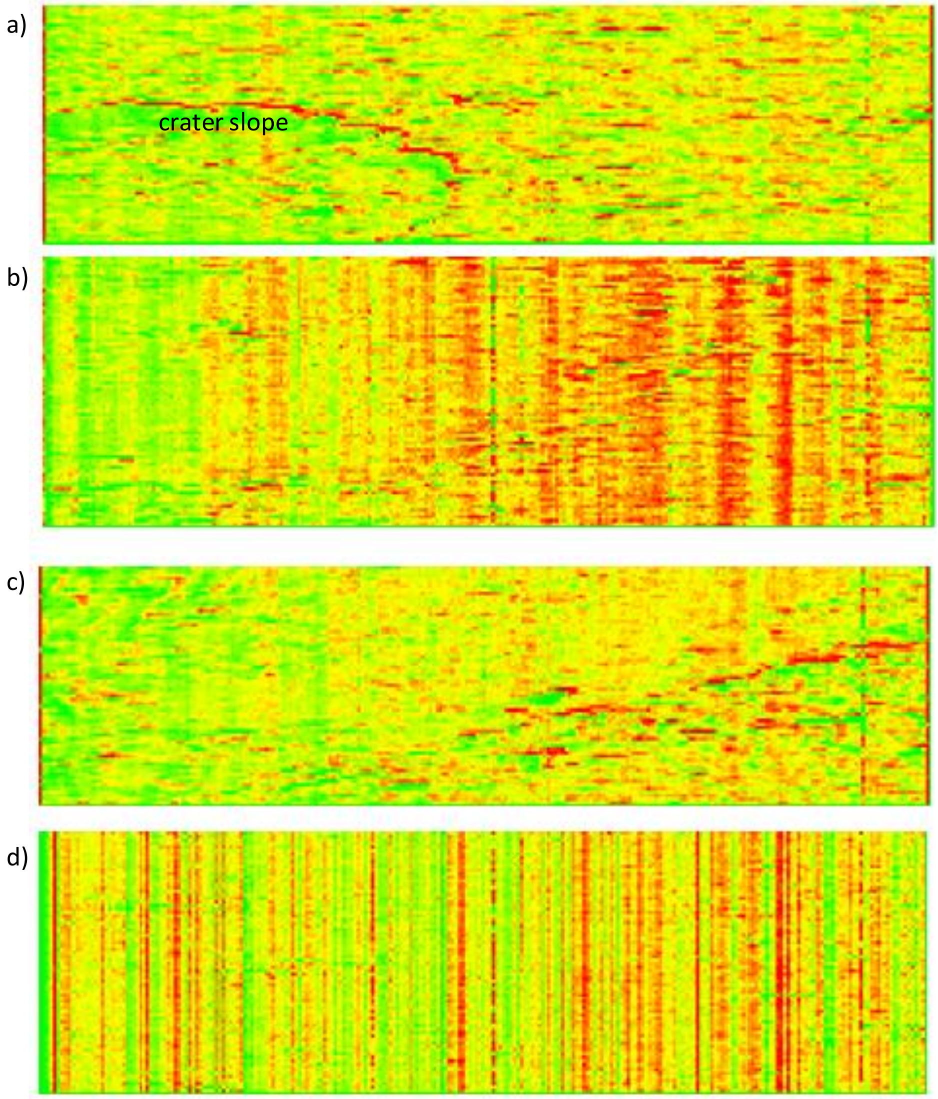

Figure 13: The BD1500_2 product shows the 1.5 μm band depth that highlights water ice. a)The image for Dantu crater shows high values in the inner slope of the crater. d)The image for Haulani crater was affected by vertical striping. a,b,c,d, show datasets for Dantu [VIR_IR_1B_1_495408230_1, VIR_IR_1B_1_494523791_1, VIR_IR_1B_1_495474811_1] and Haulani

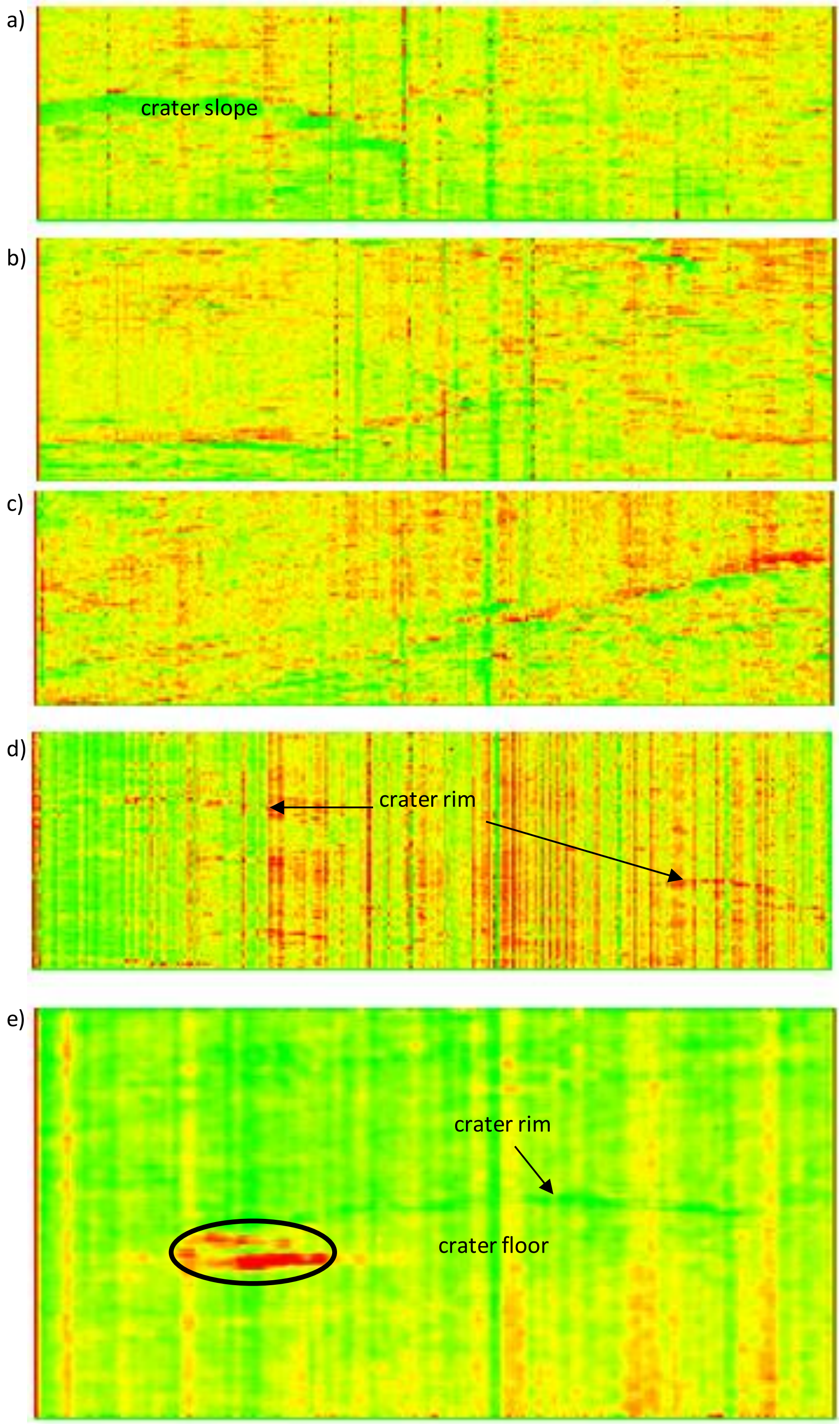

Figure 14: The BD2600 product shows the 2.6 μm H2O band that highlights water vapour. d) The crater rim of the Haulani craters and craters surrounding it can be seen. e) The central part of Occator crater shows high values. a,b,c,d,e show datasets for Dantu [VIR_IR_1B_1_495408230_1, VIR_IR_1B_1_494523791_1, VIR_IR_1B_1_495474811_1], Haulani and Occator

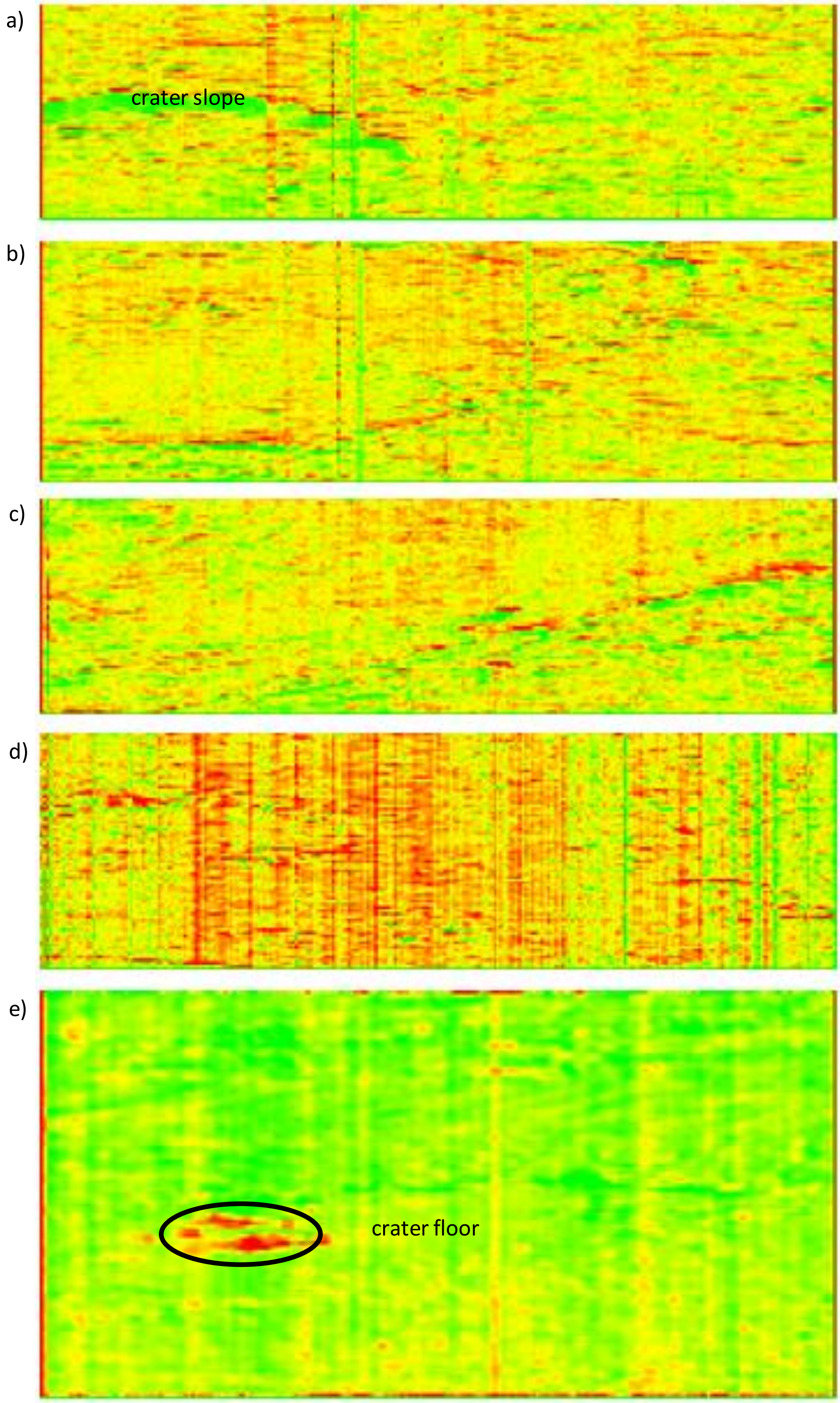

Figure 15: The ICER2 summary product highlights the 2.7 µm CO_2 ice band. a) The image for Dantu crater shows high values on the inner slope of the crater. d) High values were also seen on the crater slopes of the Haulani crater. e) High values were seen in the center of Occator crater. a,b,c,d,e show datasets for Dantu [VIR_IR_1B_1_495408230_1, VIR_IR_1B_1_494523791_1, VIR_IR_1B_1_495474811_1], Haulani and Occator

a)

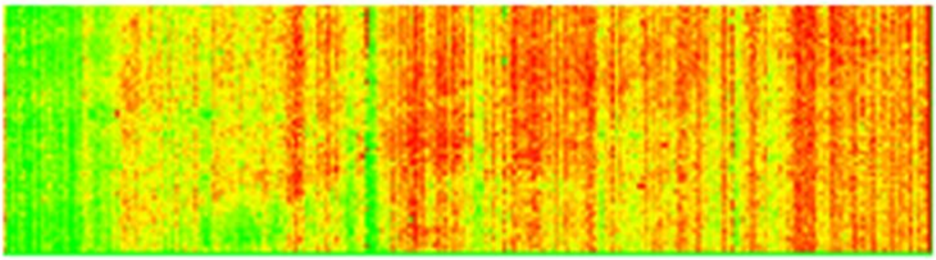

b)

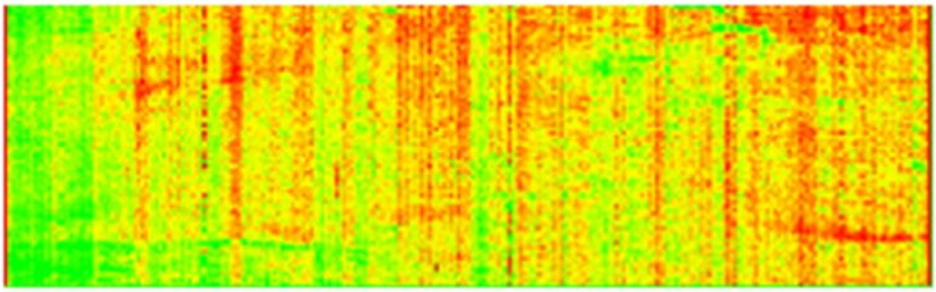

c)

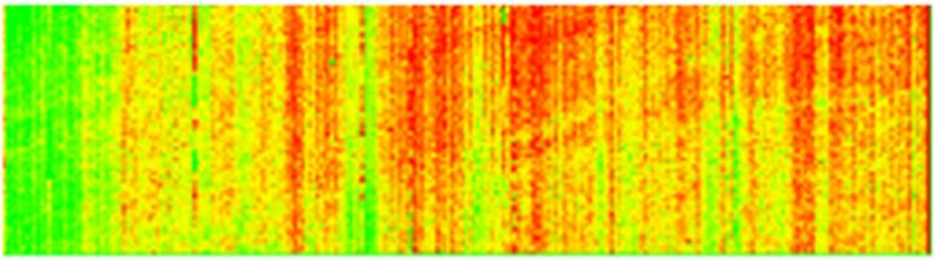

d)

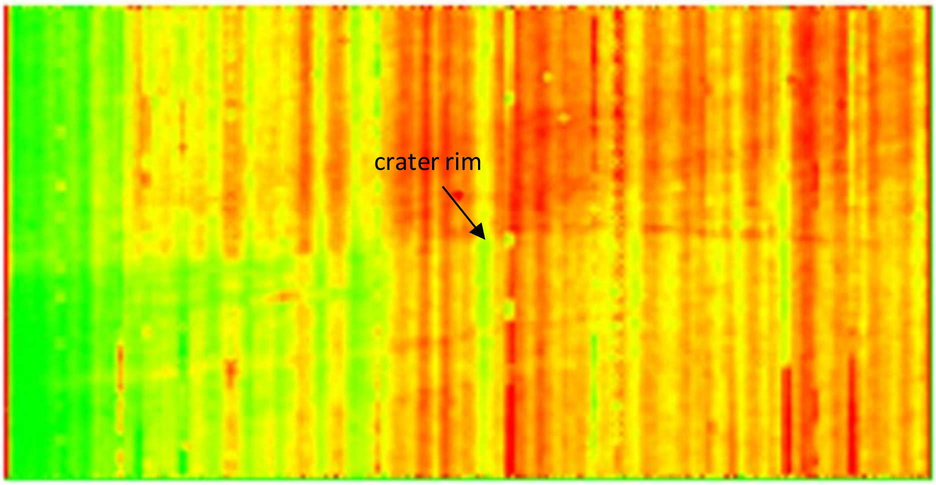

Figure 16: The BD3100 product shows the 3.1μm H2O ice band depth. e) The Occator crater itself did not show high values but the values within the crater are lower than those around it marking the crater rim prominently. a,b,c,d, show datasets for Dantu [VIR_IR_1B_1_495408230_1, VIR_IR_1B_1_494523791_1, VIR_IR_1B_1_495474811_1] and Occator

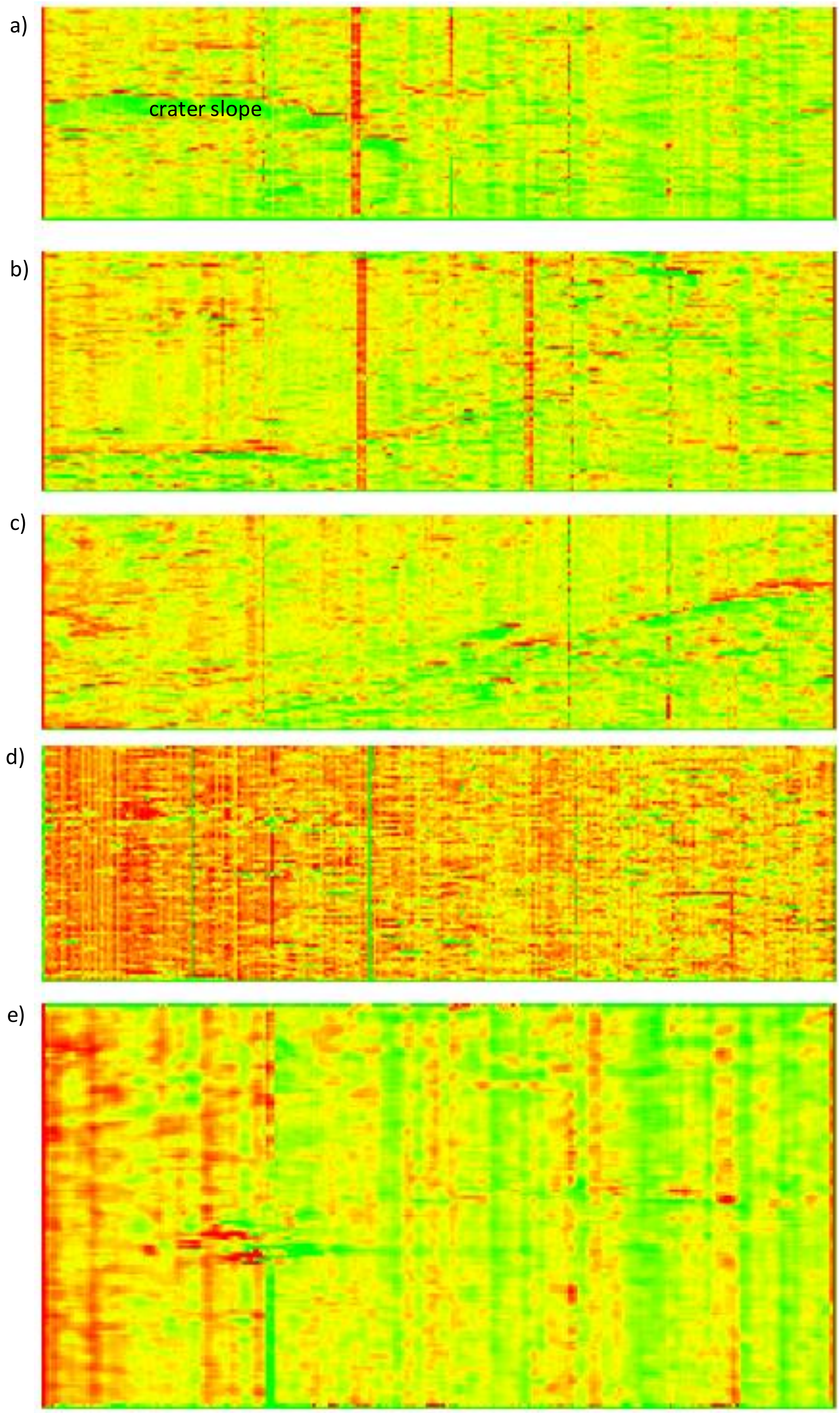

Figure 17: The MIN2295_2480 product a,b,c,d,e show datasets for Dantu [VIR_IR_1B_1_495408230_1, VIR_IR_1B_1_494523791_1, VIR_IR_1B_1_495474811_1], Haulani and Occator

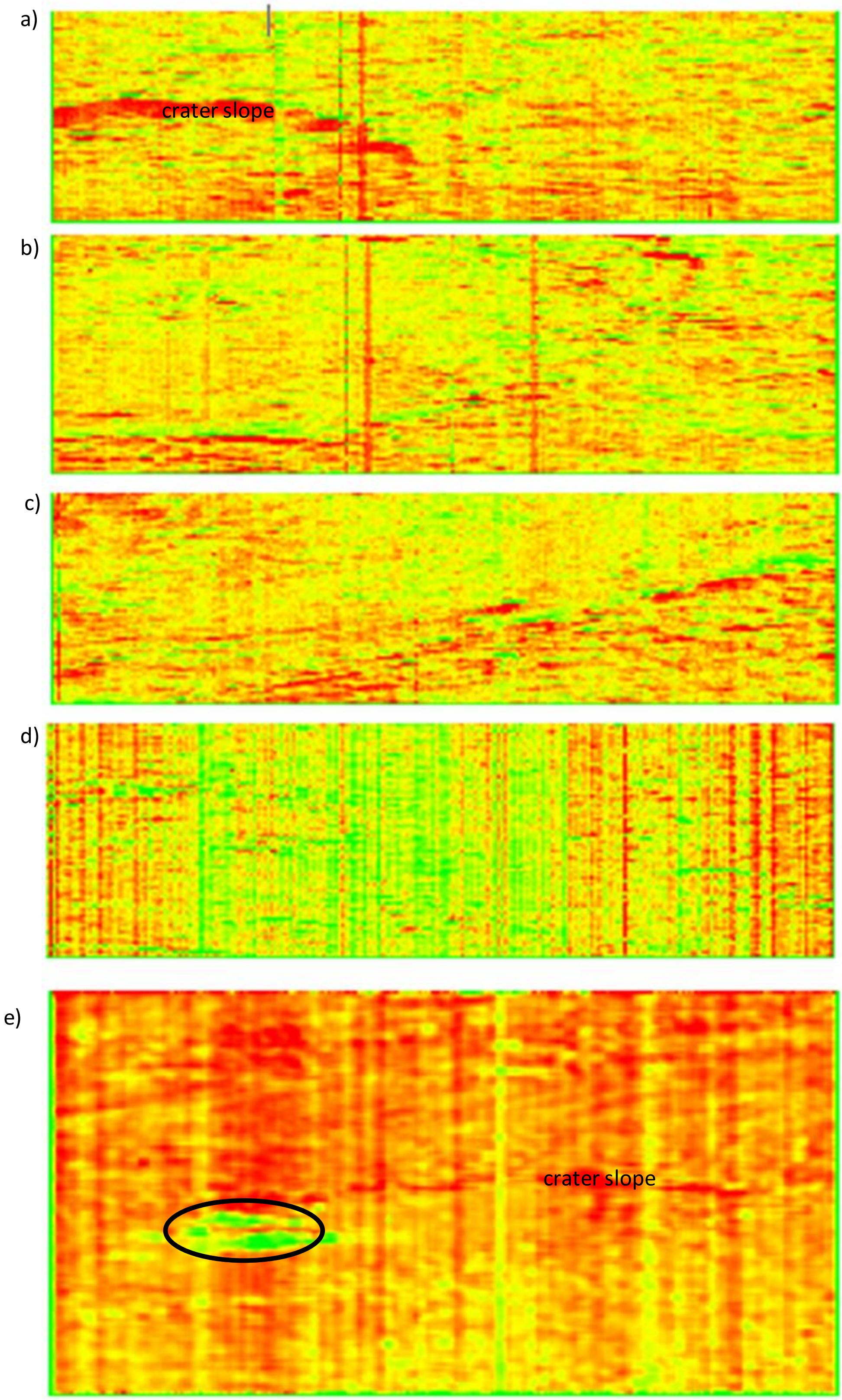

Figure 18: The MIN2345_2537 product highlights the Ca/Fe carbonate overtone band depth and metal-OH band. High values can be seen on the inner slope of the Dantu crater (a,b,c) and both inside and around the Occator crater (e). a,b,c,d,e show datasets for Dantu [VIR_IR_1B_1_495408230_1, VIR_IR_1B_1_494523791_1, VIR_IR_1B_1_495474811_1], Haulani and Occator

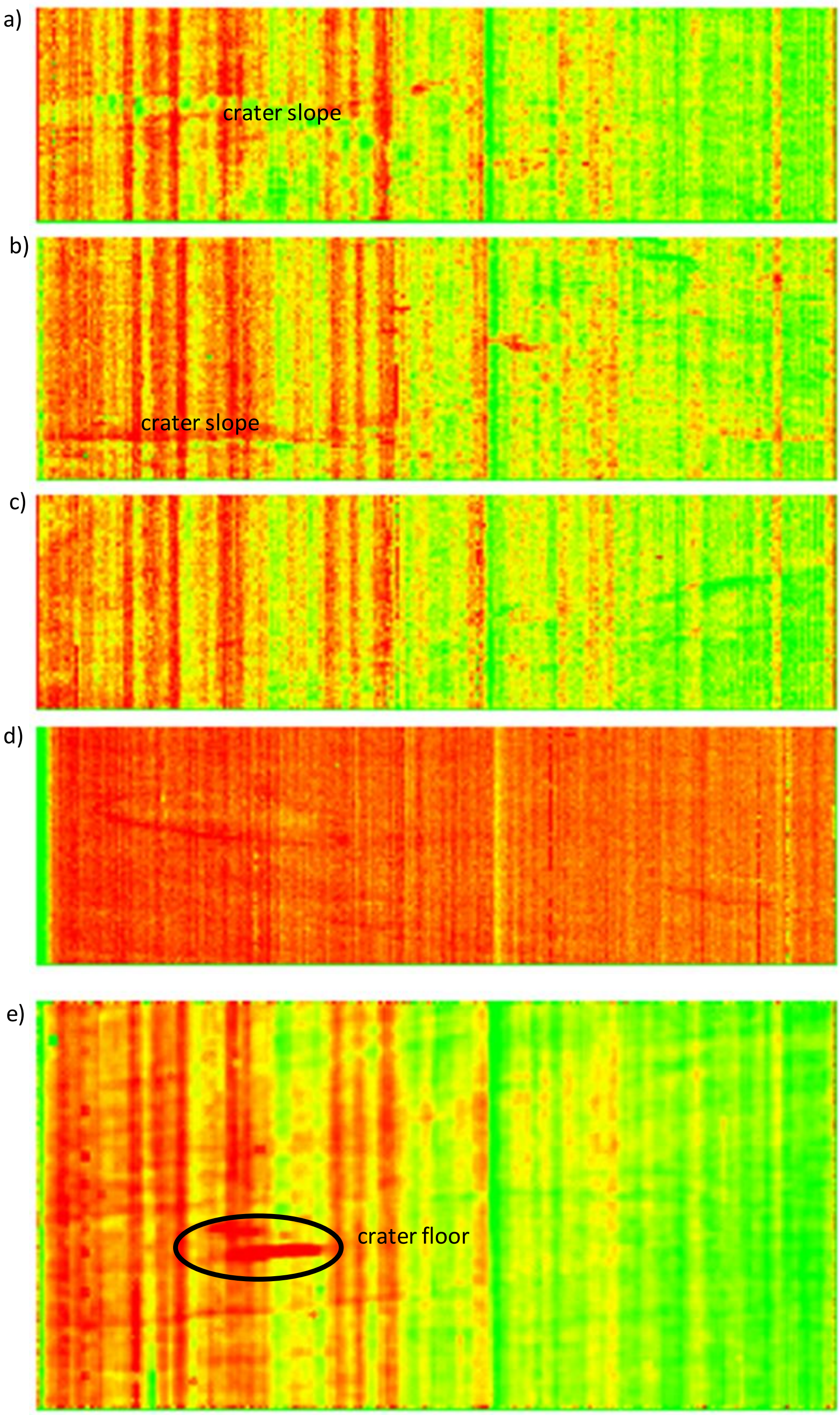

Figure 19: The BD3400_2 shows the 3.4 μm carbonate band depth. d) The Haulani crater shows high values across the entire scene. e) Image shows high values in the center of the Occator crater floor. All images show high values on their left half . The highly symmetrical nature of this region of high values indicates an artifact in the data being highlighted. a,b,c,d,e show datasets for Dantu [VIR_IR_1B_1_495408230_1, VIR_IR_1B_1_494523791_1, VIR_IR_1B_1_495474811_1], Haulani and Occator

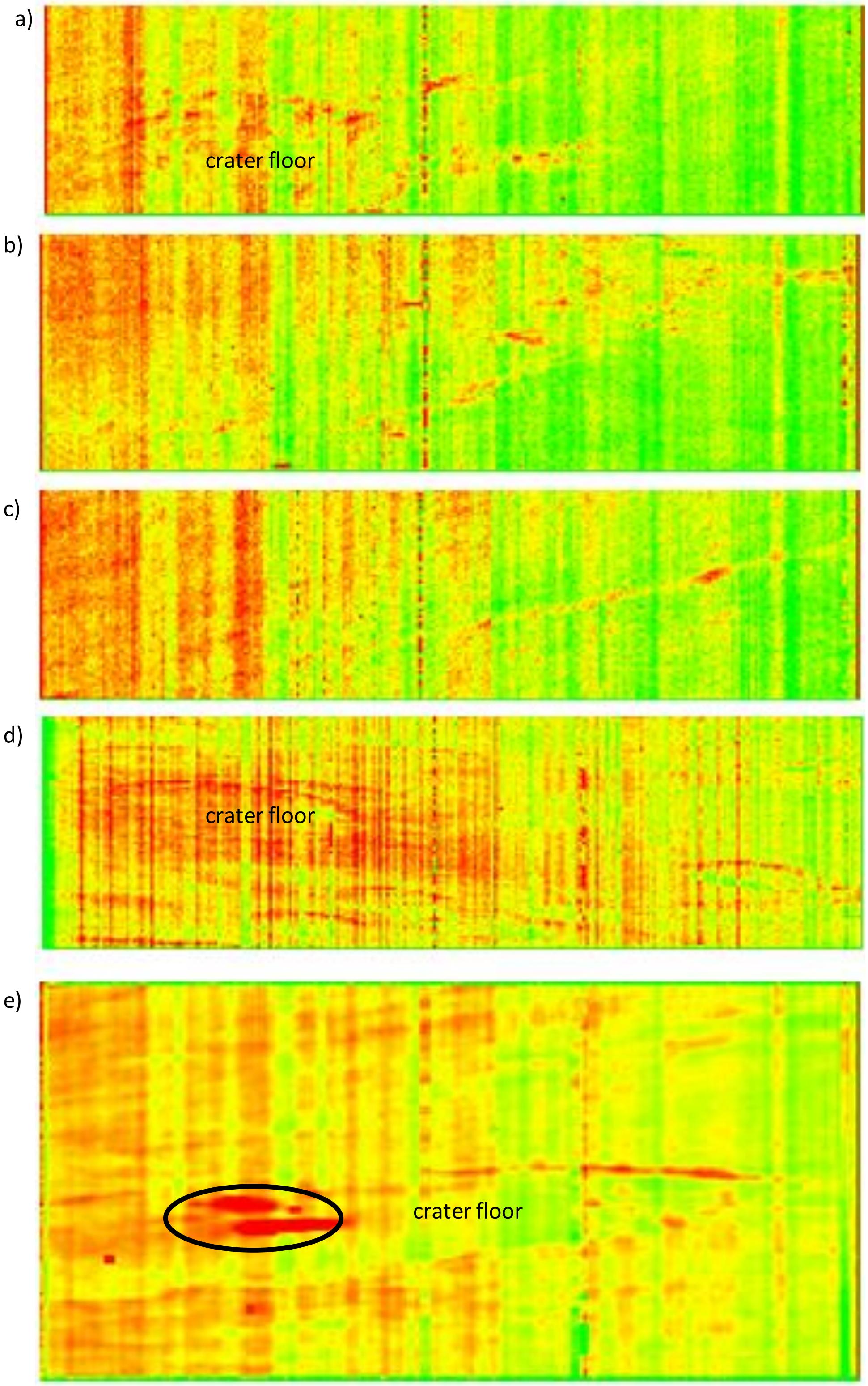

Figure 20: The CINDEX product shows the 3.9 µm carbonate index. Parts of the Dantu crater show high values (a,b,c), The Haulani crater and the region surrounding (d) it show high values. The central part of the Occator crater shows high values (e). a,b,c,d,e show datasets for Dantu [VIR_IR_1B_1_495408230_1, VIR_IR_1B_1_494523791_1, VIR_IR_1B_1_495474811_1], Haulani and Occator

3.4.2. Wavelength Mapping

The results of the wavelength mapping are shown in this sub section. The study by De Sanctis et al., (2016) identified absorption features between 2.5-4 μm for minerals used to model the Occator crater spectrum, which is why this region was used in the wavelength maps.

The first step of the wavelength mapping resulted in images of the positions and depths of the first three deepest absorption features. A scatterplot of these images was created and displayed with the results. The wavelength positions and depths were then studied from the scatterplots created during the first stage of the wavelength mapping and any distinct clusters seen in the scatterplots were further studied in another wavelength map focused on this region as in the case of the Occator crater (figure 25 & 27).

The second step resulted in a colour map and a legend, where the colour is determined by the wavelength of the absorption feature and the intensity of the colour is determined by the depth of the feature.

The spectra from the regions identified by the wavelength maps were compiled into a spectral library and compared with the RELAB spectral database[3] (Pieters, 1983). This database was chosen as it was used by De Sanctis et al., (2016) when they first modelled the spectrum of the Occator crater using various mixtures of the RELAB mineral spectra. The absorption features of the minerals identified by the previous study were expected to be identified by the wavelength mapping method along with minerals that did not get used as endmembers during the spectral modelling methods used by those studies. Comparisons of the spectra obtained and the spectra from De Sanctis et al., (2016) will be discussed in chapter 4.

[3] http://www.planetary.brown.edu/relab/

3.4.2.1. Dantu Crater -VIR_IR_1B_1_495408230_1

The wavelength range used was from 2.5-4 µm. The wavelength map (figure 21a) shows the wavelength of the deepest absorption feature between 3-3.2 µm and the region around the crater showed the presence of this feature. The scatterplot of the minimum wavelength and depth shows a cluster between 3-3.1 µm (figure 21c). The average spectrum of pixels from the encircled region in the center of the crater show this absorption feature at 2.73 µm. The average spectra of pixels from these regions (figure 21d) shows the position of the absorption feature for region B at 3.19 µm.

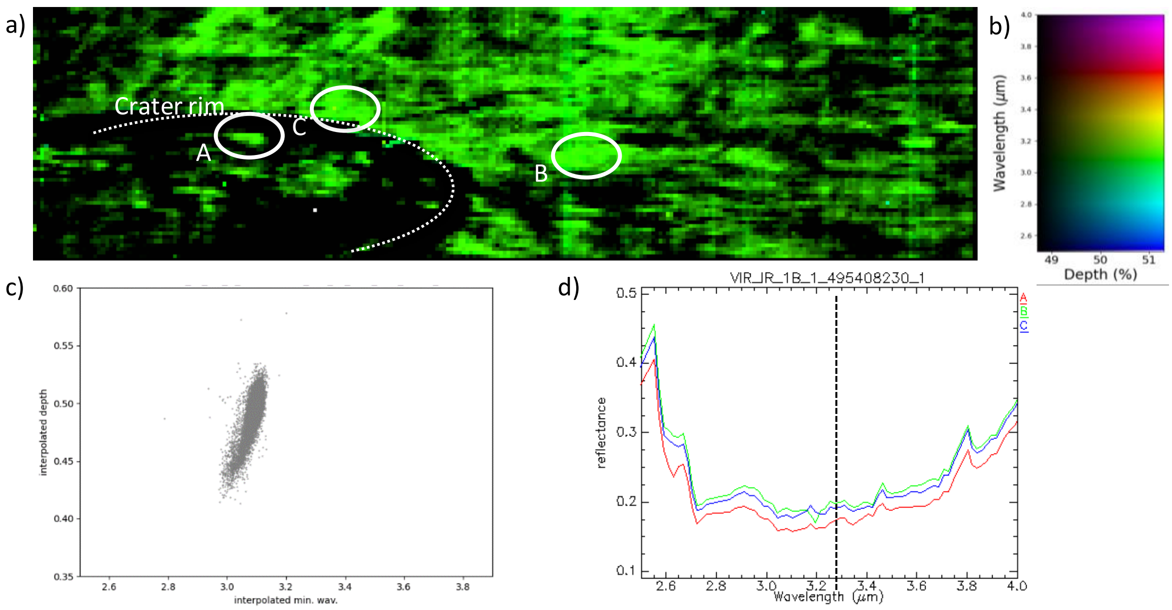

Figure 21: The wavelength map for the range 2.5-3µm for the Dantu crater (VIR_IR_1B_1_495408230_1) showing the 3 regions where spectra were extracted. Green regions correspond to a wavelength range between 3-3.2µm. b) legend for the wavelength map. c) Scatterplot for the minimum wavelength and depth of the deepest absorption feature for the entire image showing a cluster between 3-3.2µm. d) Average spectra for pixels in the 3 encircled regions in image a) showing absorption feature for B at 3.19 µm.

3.4.2.2. Dantu Crater -VIR_IR_1B_1_494523791_1

The wavelength map for wavelength range 2.5-2.9 µm (figure 22a) shows a spectral absorption feature at 2.73 µm was prominent in the center of the crater as well as along its rim. The scatterplot of the minimum wavelength and depth shows a cluster between 2.7 and 2.75 µm (figure 22c). The average spectrum of pixels from the encircled region in the center of the crater show this absorption feature at 2.73 µm.

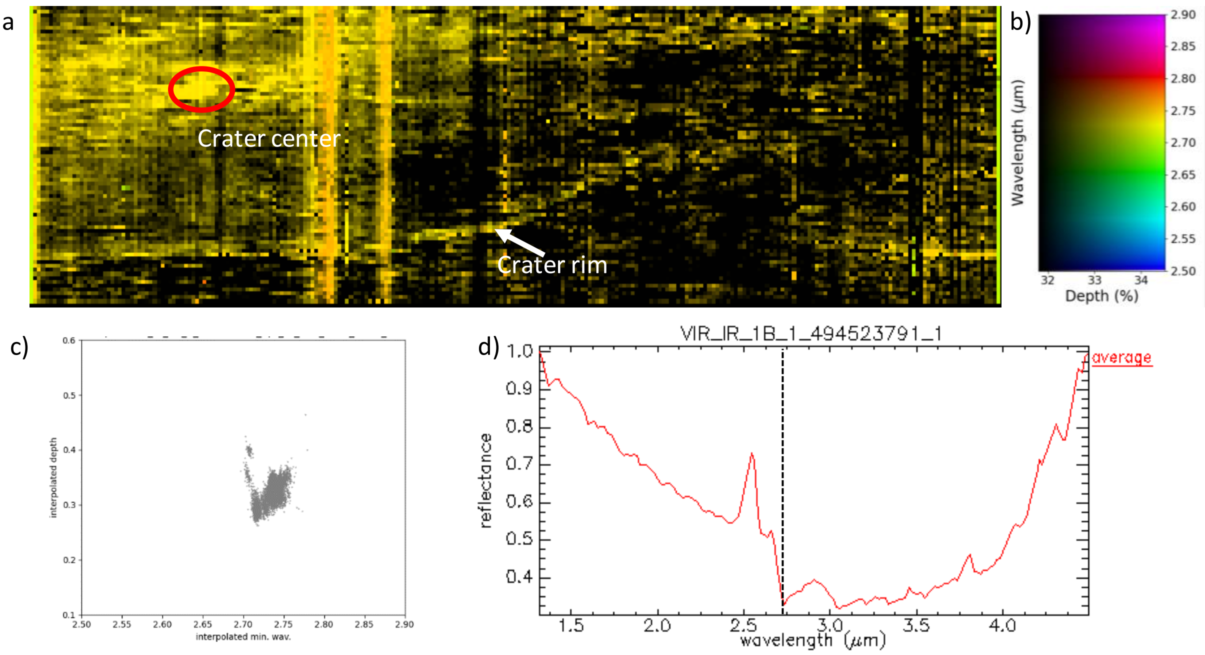

Figure 22: a) The wavelength map for the range 2.5-2.9 µm for the Dantu crater (VIR_IR_1B_1_494523791_1) yellow regions correspond to a wavelength range between 2.7-2.75 µm. b) legend for the wavelength map. c) Scatterplot for the minimum wavelength and depth of the deepest absorption feature for the entire image shows a cluster between 2.7-2.75µm. d) Average spectrum for pixels in the encircled region at the center of the crater in image a); deepest feature location at 2.73 µm shown as a dotted line.

3.4.2.3. Dantu Crater- VIR_IR_1B_1_495474811_1

The wavelength range from 2.5-3.9 µm was used. The wavelength map is shown in figure 23a which shows the deepest absorption feature between 3.1 and 3.2 µm. The inner slopes of the crater showed the presence of this feature as well as parts of the crater floor. The scatterplot of the minimum wavelength and depth showed a cluster between 3.1-3.2 µm (figure 23c). The average spectrum of pixels from the encircled region along the inner slope of the crater showed the absorption feature between 3.1-3.2 µm (figure 23d).

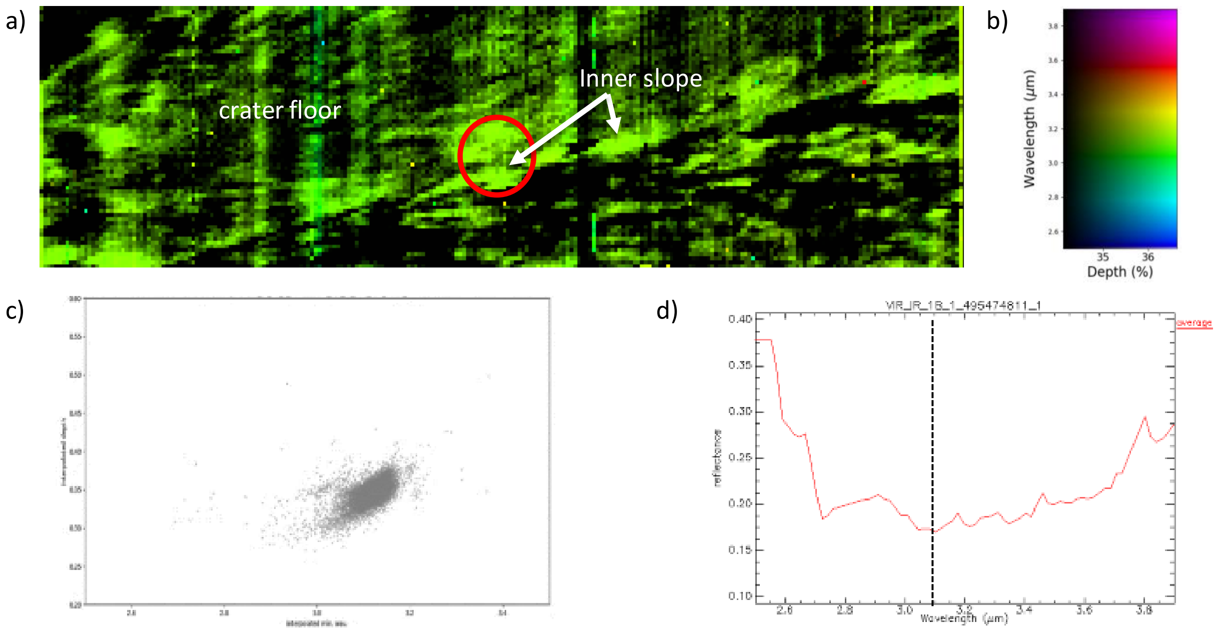

Figure 23: The wavelength map for the range 2.5-3.9 µm for the Dantu crater (VIR_IR_1B_1_495474811_1). Green regions correspond to a wavelength range between 3.1-3.2µm. b) legend for the wavelength map. c) Scatterplot for the minimum wavelength and depth of the deepest absorption feature for the entire image showing a cluster between 3.1-3.2µm. d) Average spectra for pixels in the encircled region of the inner slope of the crater in image a).

3.4.2.4. Haulani Crater - VIR_IR_1B_1_494731110_1

The wavelength range from 2.5-3.9 µm was used. The wavelength of the deepest absorption feature seen in the wavelength map (figure 24a) was at 3 µm as indicated by a green colour in the legend. This feature was prominent on a part of the Haulani crater floor as well as in smaller craters beside it. Some regions showed an absorption feature at 2.7 µm and appeared as blue regions in the map. The scatterplot of the minimum wavelength and depth showed two clusters, the first between 2.7-2.9 µm and the second between 2.9-3.1 µm (figure 24c). In the average spectrum of pixels from the three encircled regions in figure 24a, A showed a higher reflectance than B and C and was likely indicative of a facula. All three spectra showed features at 2.7 and 3.1 µm.

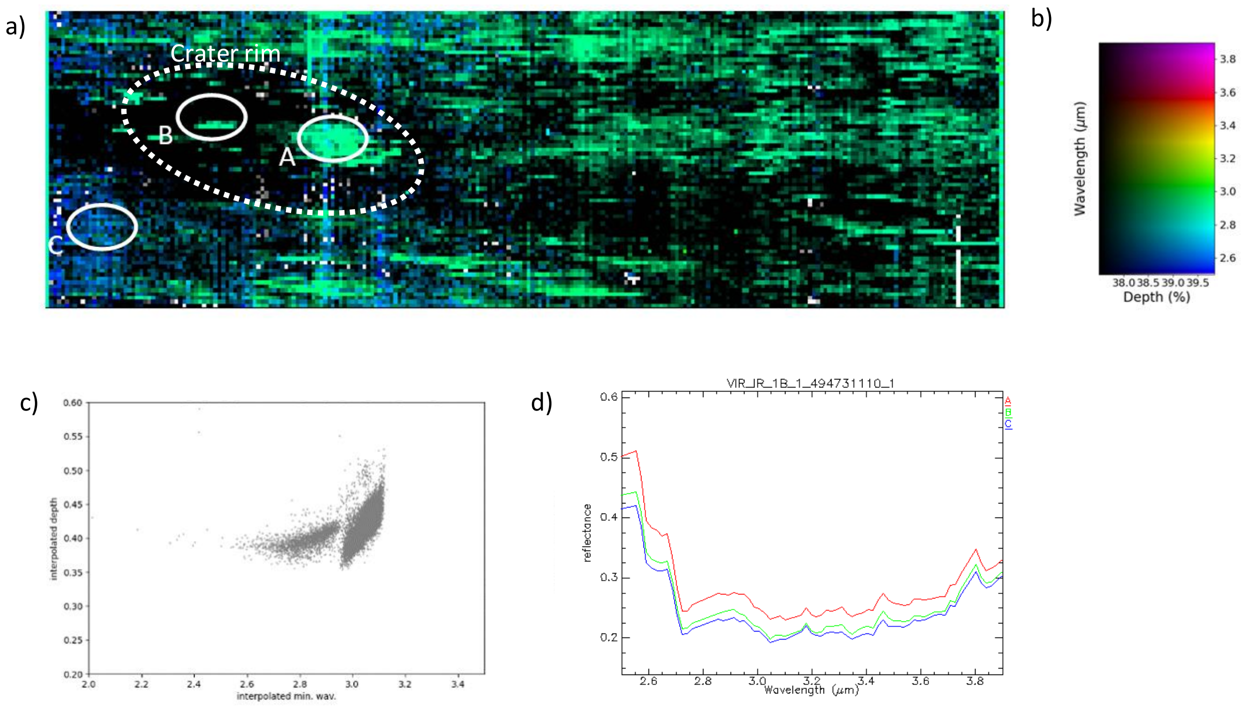

Figure 24: a) The wavelength map for the range 2.5-3.9 µm for the Haulani crater (VIR_IR_1B_1_494731110_1) showing the 3 regions where spectra were extracted. Green regions correspond to a wavelength range between 2.8-3µm and blue regions correspond to wavelength range 2.6-2.8 µm. b) legend for the wavelength map. c) Scatterplot for the minimum wavelength and depth of the deepest absorption feature for the entire image showing a cluster between 3-3.2µm. d) Average spectra for pixels in the 3 encircled regions in image a) showing absorption features at 2.7 and 3.1 µm.

3.4.2.5. Occator Crater- 2.5-3.9 µm

The wavelength range from 2.5-3.9 µm was used. The deepest absorption feature was at 3 µm and was seen at the center of the crater floor, along some parts of the inner slope of the crater and in the regions surrounding the crater in a striated pattern (Figure 25). The spectra for region A were very different and are shown separately as well in figure 26. The scatterplot of the minimum wavelength and depth showed two clusters, the first between 2.7-2.9 µm and the second between 2.9-3.1 µm (figure 25c). In the average spectrum of pixels from the three encircled regions in figure 25a, A showed a feature at 3.19 µm.

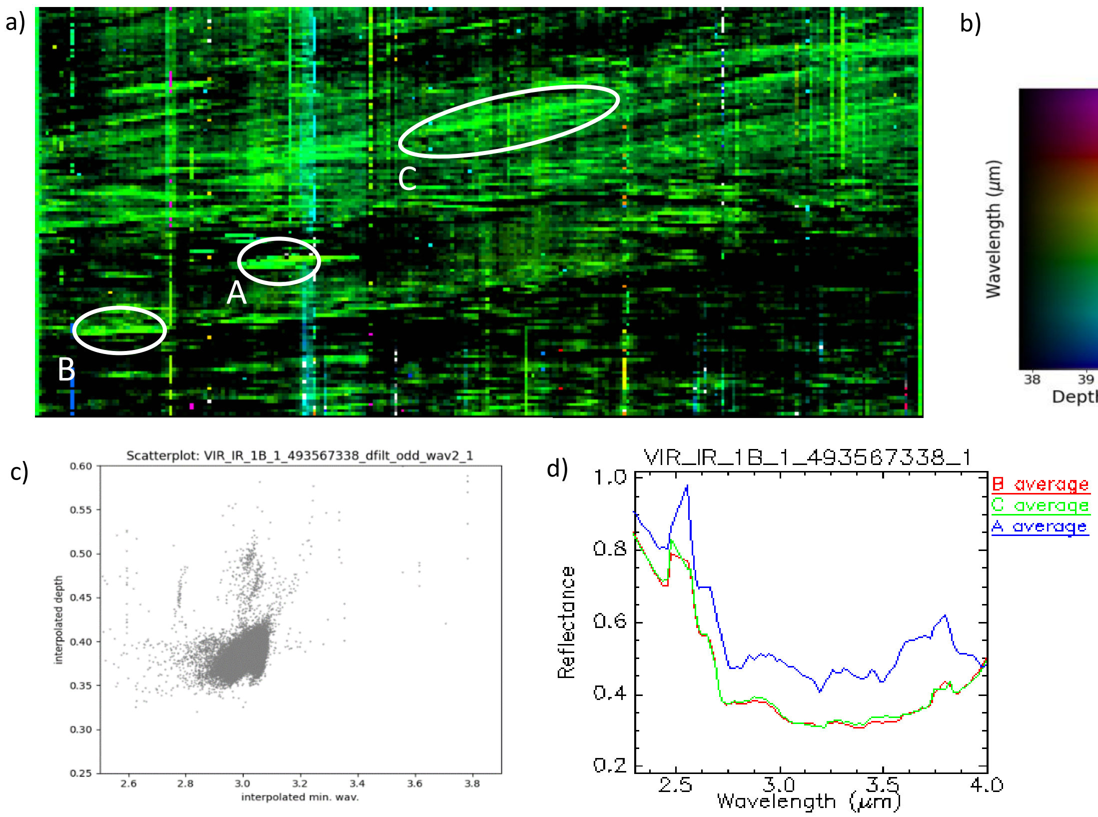

Figure 25: The wavelength map for the range 2.5-3.9 µm for the Occator crater (VIR_IR_1B_1_493567338_1) showing the 3 regions where spectra were extracted. Green regions correspond to a wavelength range between 3-3.2µm. b) legend for the wavelength map. c) Scatterplot for the minimum wavelength and depth of the deepest absorption feature for the entire image showing a cluster between 2.9-3.1µm. d) Average spectra for pixels in the 3 encircled regions in image a).

The spectrum for region A showed a higher reflectance than B and C and the depth of the features were also greater which is why the invidual pixel spectra from this region were studied for possible mineral variability.

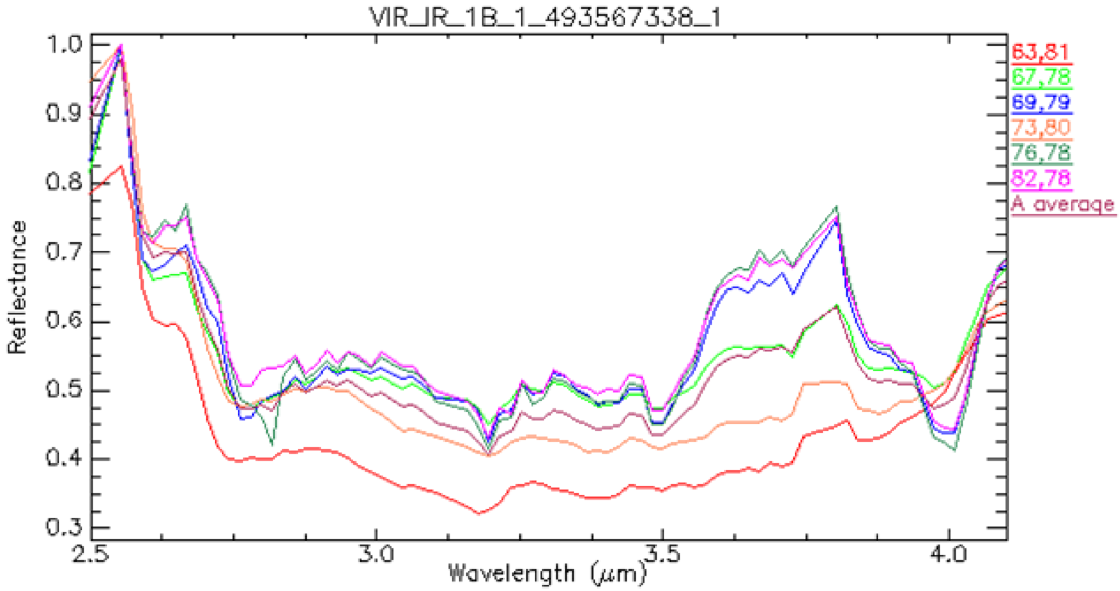

Figure 26: The spectra for pixels from region A at the center of the Occator crater floor. Distinct absorption features are seen at 3.19, 3.5 and 4 μm.

3.4.2.6. Occator Crater- 3.9-4.5 µm

The wavelength range from 3.9-4.5 µm was used to create the wavelength map in figure 27a. The wavelength range used was narrow, but the scatterplot of the minimum wavelength and depth showed distinct clusters in this range at 4 µm, between 4.1-4.2 µm and between 4.2-4.3 µm (figure 27c). The deepest absorption feature was at 4 µm in the center of the Occator crater (also seen in figure 25). Most of crater floor had absorption features at ~4.1 µm as well as some striated parts in the surrounding regions. In the average spectrum of pixels from the three encircled regions in figure 25a, A showed a higher reflectance than B and C and was likely indicative of a facula. All three spectra showed features at 2.7 and 3.1 µm.

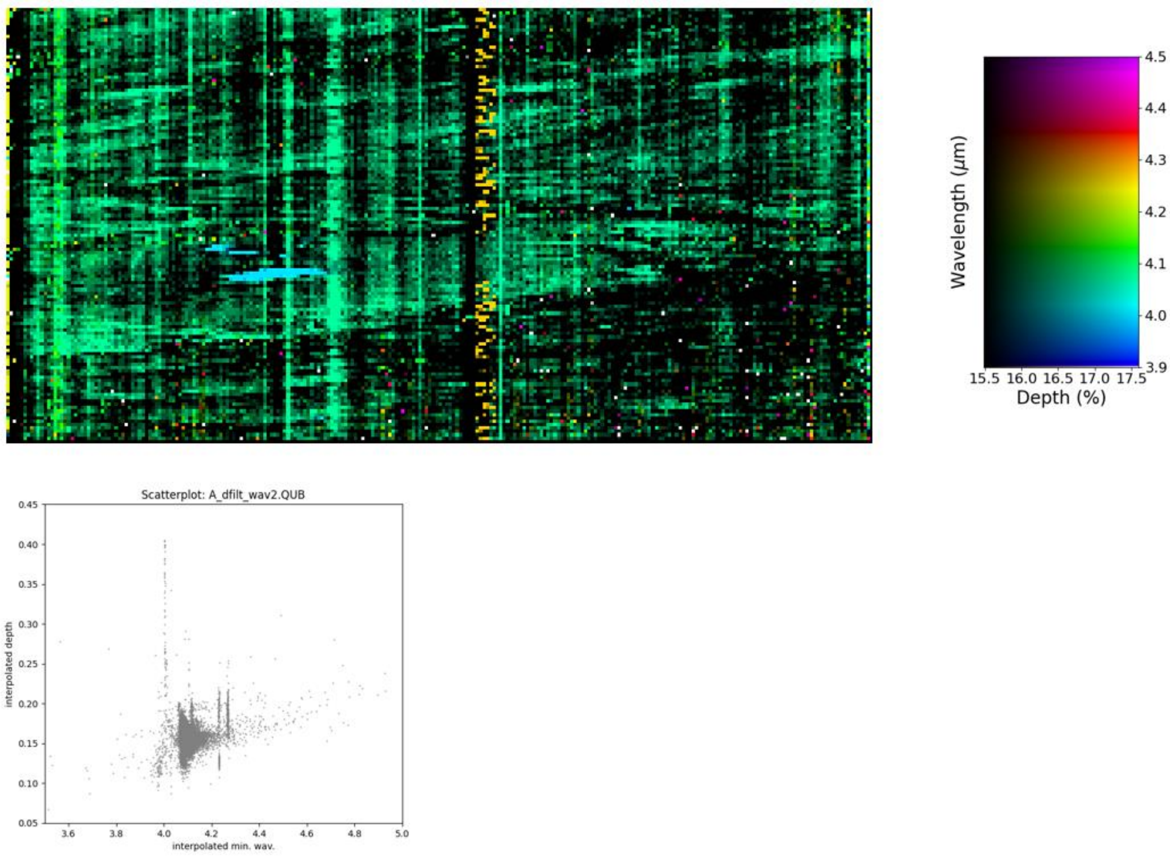

Figure 27: The wavelength map for the range 3.9-4.5 µm for the Occator crater showing two different regions at wavelength positions 4.05 µm and 4.1 µm. The orange band at ~4.3 µm is an artifact affecting the image samples (columns). b) Scatterplot for the minimum wavelength and depth of the deepest absorption feature for the entire image. The spectra are the same as that in figure 18 c and figure 19.

3.5. Photometric correction and map projection in ISIS3

The datasets were map projected after the photometric correction was done in ISIS3 and the ISIS cube files (.cub) were exported into QGIS. The resulting mosaics for Dantu crater can be seen in figure 28 and the images for Occator and Haulani craters in figure 29. ISIS does not carry out the artifact removal procedure which is why a white stripe can be seen across the images.

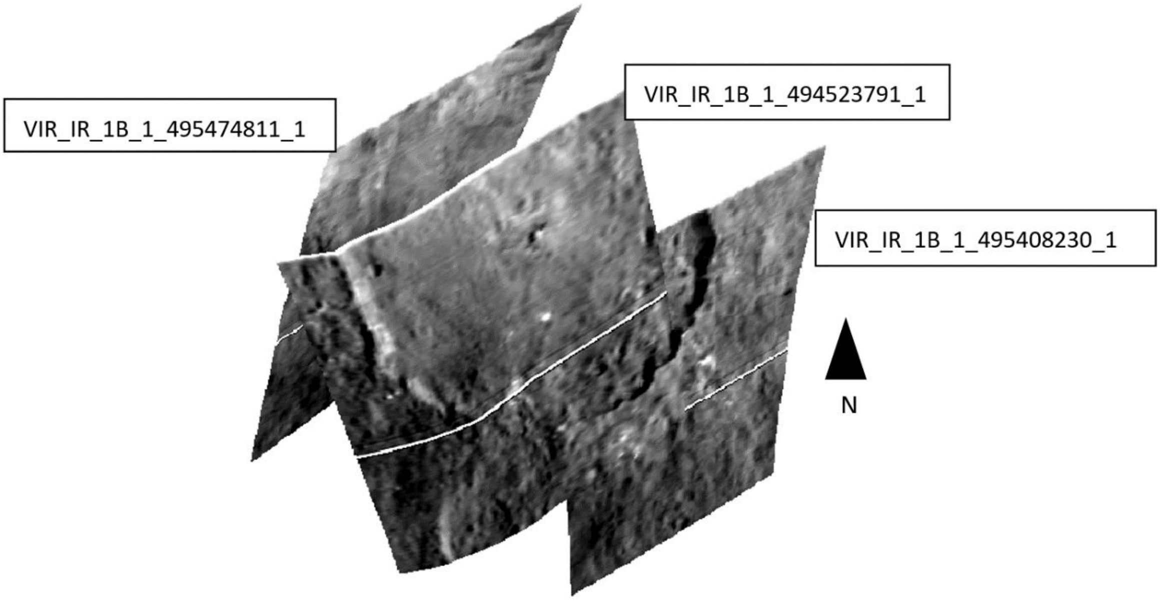

Figure 28: The Dantu crater VIR datasets mosaic

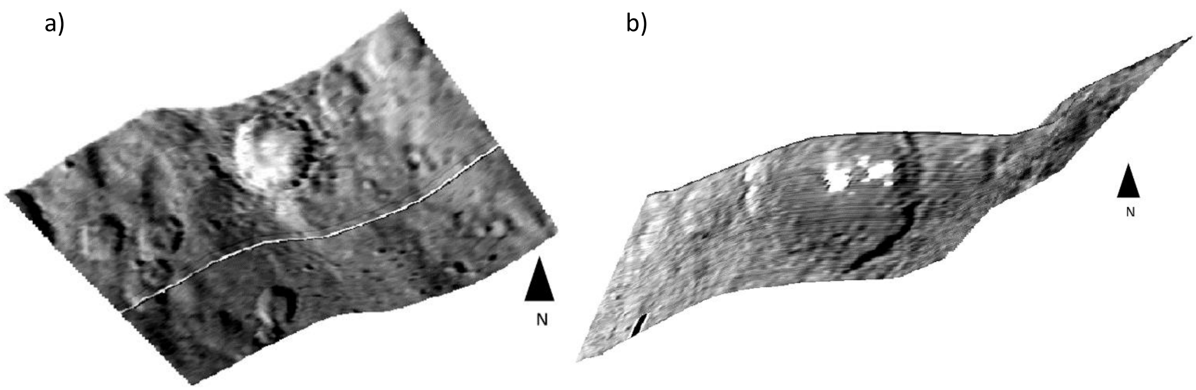

Figure 29: a) The Haulani crater and b) the Occator crater VIR dataset

4. DISCUSSION

The primary objective of this research was to investigate the nature of brine pockets on Ceres using hyperspectral imagery to study the mineral deposits on the surface. It aimed to use a method that did not involve reconstructing the average surface spectrum using mixtures of various spectral endmembers. The results for each step of the process will be discussed.

4.1. Data Preprocessing

The standard procedure to study multispectral or hyperspectral images involves radiometric correction followed by solar correction, atmospheric correction, photometric correction and map projection after which the spectral analyses are carried out. A thermal correction was not carried out because I had not intended to use the thermal infrared bands during the spectral analysis. In the case of the Dawn datasets, the radiometric correction and solar correction were carried out followed by an additional ground correction which targeted the bands that were later removed due to the presence of spectral artifacts. Ceres does not have an atmosphere which is why an atmospheric correction was not carried out. To carry out a photometric correction and map projection, a digital elevation model is needed but an attempt to carry out these steps in ENVI resulted in a distorted image. Surface studies on Ceres use the ISIS software designed by USGS specifically for the analysis of datasets collected by various space missions. These steps were then carried out in ISIS3. An issue faced during this stage was that ISIS requires all input datasets to be converted into an ISIS cube with a .cub format. To do this the software requires the all the files listed in table 1, which is why files processed in HypPy or ENVI cannot be opened in ISIS. Files modified in ISIS on the other hand can only be exported as an image file and hence they cannot be use as a hyperspectral cube for spectral analysis in ENVI or HypPy. Due to these issues, the spectral analysis was carried out on datasets that were not photometrically corrected or map projected. This deviation from the standard preprocessing procedure may result in errors in the spectral analysis due to topographic effects but this was kept in mind during the interpretation of the results.

4.2. Data Quality Assessment and Artifact Removal

The datasets showed the presence of spectral artifacts which had to be removed before a spectral analysis could be carried out. Studies that use the Dawn VIR data all carry out an artifact removal procedure as described by Carrozzo et al. (2016) which targets saturated pixels, spectral spikes and vertical striping. In addition to the paper, a part of the code was made available on the PDS archive in the VIR_CALIBRATION document which states that the artifact removed dataset would be made available in the PDS archive as the DAWN-A-VIR-3-RDR-IR-CERES-AR-SPEC-V1.0 data in 2017, but this dataset was not found. I was not able to complete the code correctly and could not employ it in my preprocessing stage. The steps carried out by the code were vital to the preprocessing which is why alternative steps in ENVI and HypPy were devised (as explained in section 2.3) to carry them out. These steps led to a satisfactory artifact removed cube which can be seen in the data statistics before and after the artifact removal step (figure 30). Any further processing- like median filtering was found to alter the spectra to an extent that might remove spectral information given that the reflectance values were not very high. The spectra after the preprocessing and artifact removal are visually comparable to the spectra seen in previous studies (Carrozzo et al., 2016; De Sanctis et al., 2016).

a) b)

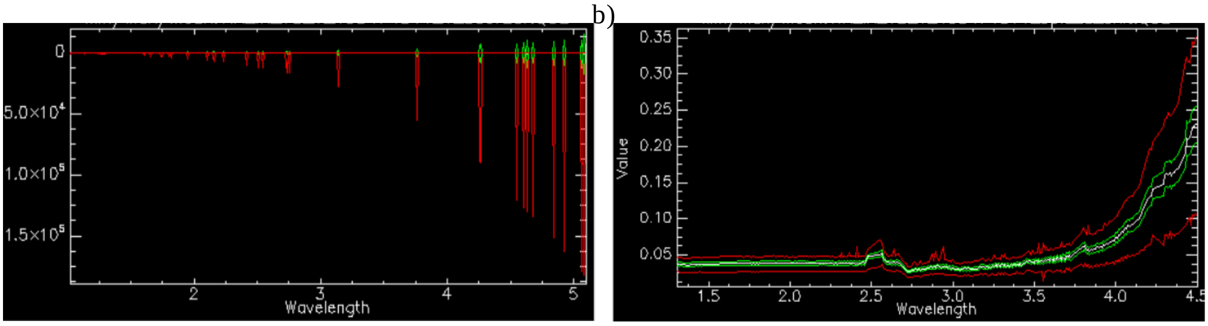

Figure 30: Band statistics for VIR_IR_1B_1_494523791_1 before and after the artifact removal step.

The VIR_CALIBRATION document also contains the locations of defective pixels which are to be removed during the artifact removal procedure. This list was compared to the pixels flagged by HypPy's destriping filter but the two did not match. This could be because of the thresholds set for the destriping filter, however, even regions with adjacent bad samples across multiple bands were not listed even though they are present in all the datasets which can be seen very distinctly in the summary products. The list in the calibration document was not made for a specific datacube but a general list for the instrument, while the artifact removal procedure in this study was carried out on each datacube which could also explain why it was more detailed.

The bands in the thermal infrared region after band 370 (4.5µm) were affected by striping to a higher extent. A likely cause for this could be pronounced sensitivity differences between adjacent rows of the charge coupled device (CCD) of the VIR spectrometer (Barducci and Pippi, 2001; Gómez-Chova et al., 2008) in this wavelength range. The spectra also show higher reflectance values after 3.5 µm due to thermal emission from the surface. I believe an artifact removal procedure tailored specifically to these bands would yield better results but wasn't carried out during this study as I did not plan to use the thermal bands for the spectral analysis. These bands were removed during the spectral subsetting.

The odd-even band effect seen in the spectra made it impossible to use wavelength mapping. A simple solution was devised to remove it- create two subsets, one for the odd bands and one for the even bands. This resulted in a smooth spectrum. The artifact removal procedure by Carrozzo et al., (2016) calculated a weighted average of each channel with its two adjacent channels resulting in a cube with all its bands and a minimised odd-even band effect. This step could not be carried out in ENVI or HypPy as it would involve having to calculate this average for each of the 432 bands in the dataset individually, which while possible would take up a lot of time and hence was avoided.

4.2.1. Discrepancy between ENVI/ HypPy and ISIS

The datacubes downloaded from the PDS archive show different values for the cluster of pixels at the center of Occator crater. ENVI and HypPy show these pixels as having negative values but ISIS3 does not (figure 31). It is unclear as to what is causing this difference since the same dataset was viewed without any processing being carried out on it. This region shows interesting features in the summary products and wavelength maps and is also the location of the crater faculae as stated in previous studies.

a)

b)

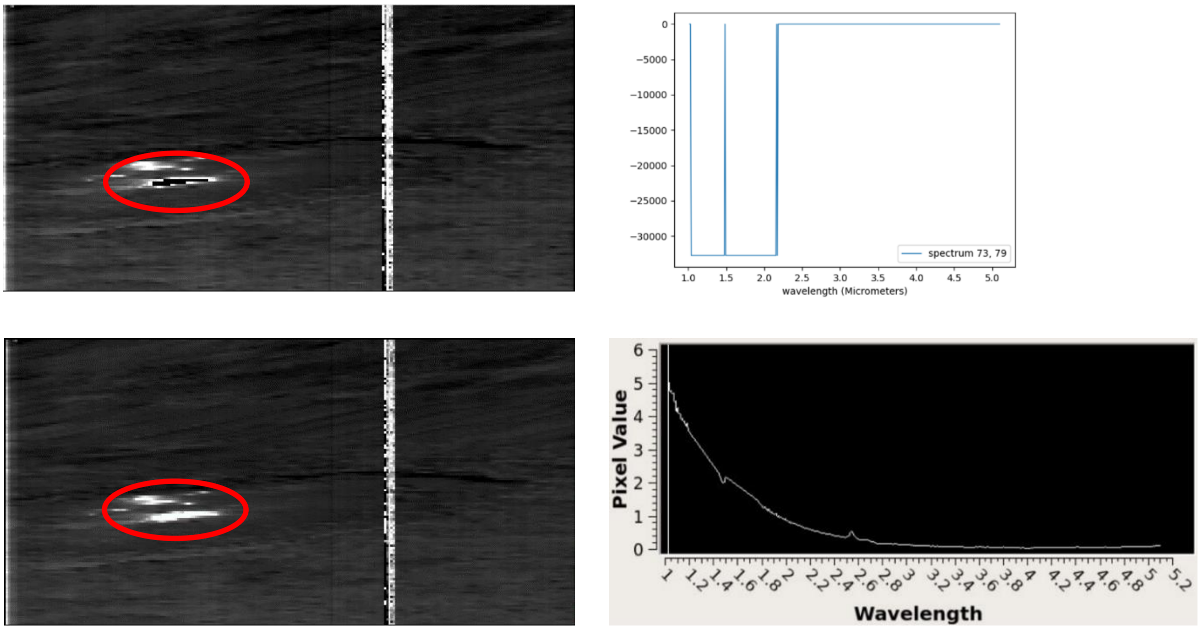

Figure 31: Differences between the same image of band 61 and spectrum of pixel (73,79) in a) HypPy and b) ISIS.

4.3. Spectral Analysis

The summary products that showed interesting patterns were those targeted at analysing H_2O /CO_2 ice and carbonates. Two products focus on the H_2O ice band depth at 1.5 µm and 3.1 µm, and one product on the CO_2 ice band depth at 2.7 µm. The RELAB spectra for carbonates comprised mainly of dolomite ($CaMg(CO_3)_2$), Mg carbonate, Ca/Fe carbonate and natrite (Na_2CO_3) were used to compare the results of this with as they were used in previous studies to model the Occator crater spectrum. The results of the summary products and wavelength maps will be discussed for each crater in the following section.

4.3.1. The Occator crater

The BD3100 product (figure 15e) showed a clear demarcation between the crater floor and the surrounding terrain, with the surroundings and the inner slope of the crater having a higher value than the crater floor. This product did not indicate the presence of any prominent features at the center of the crater, which was seen in both the ICER2 product (figure 14e) and the BD2600 product (figure 13e). In contrast to the central feature, the rest of the crater floor and the surrounding regions showed much lower values in these two products. The BD2600 product detects H_2O vapour present in the atmosphere and it showed high values in the center of the Occator crater (figure31a). The R440 summary product which indicates the presence of clouds or haze was studied to verify the result of the BD2600 product and it also showed high values in the same region (figure31b). Both these products provide information about the atmosphere. Ceres, a dwarf planet with low gravity does not have an atmosphere, yet these products showed high values albeit only at the center of Occator crater.

a)
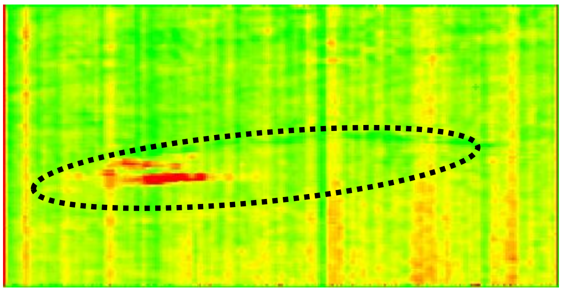
b)
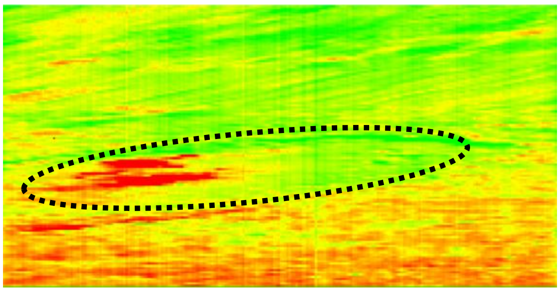

Figure 33: High values seen at the center of Occator crater for a) the BD2600 product for water vapour in the atmosphere and b) the R440 product for clouds or haze. The dotted line shows the crater outline.

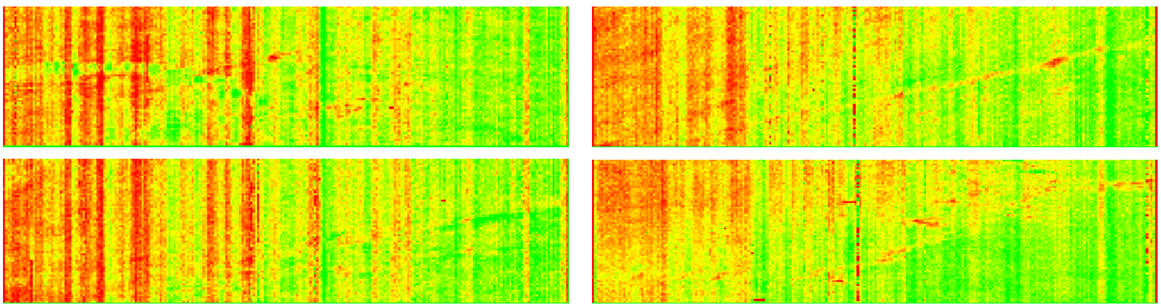

Figure 32: The left part of all four images shows a region with high values.

The presence of water vapour on Ceres was discovered in 2014 around the mid latitudes of Ceres (Küppers et al., 2014); Nathues et el., (2015) noted that this coincided with bright regions on Occator crater and concluded that it was produced by a haze of H_2O ice and dust. The summary products were able to identify water vapour accurately and could be used to explore more locations with these features in the future.

Both the BD3400_2 and CINDEX products showed high values in one half of the image (figure 32) although I believe this was due to a sensor defect as this divide has an unnaturally symmetrical nature that would not be produced by a naturally occurring deposit or geomorphological feature. Both products highlighted the central feature in the crater which had much higher values than the other parts of the images. The inner slope of the crater also has high values in the CINDEX product as well as a small cluster of pixels centred at (21,89).

The faculae are present in the central region of the Occator crater and models for the formation of the faculae deposits suggest that the brine fluids are extruded like a "salt-water fountain" and flash freeze on the surface (Ruesch et al., 2019). This could explain the detection of CO_2 ice and water vapour at the time the datacube was created. It would have to be supported by images taken of the faculae around the same time frame. The pixels from the central region also have negative values in bands 1-125 (1.02-2.20 µm). The reason for these negative values is unknown however the spectra for the remaining bands do not show any issues and these bands were used to create the summary products

It is also important to note that this study does not carry out an atmospheric correction due to the lack of an atmosphere on Ceres that could affect the spectral analysis like on Earth or Mars. A more conclusive statement could be made on the presence or absence of water vapour from the results obtained in this study after this correction is performed and the BD2600 summary product is reproduced.

The MIN2345_2537 product (figure 33b) showed high values for the entire image except the crater's center. It clearly highlighted a narrow part of the central region which had values similar to the crater floor indicating a gap between the faculae which can be seen in framing camera images.

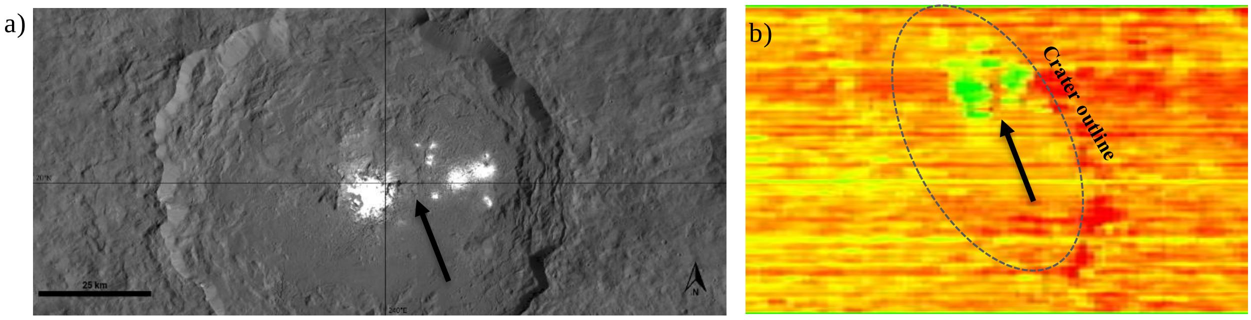

Figure 34: The gap between the floor faculae as seen in a) the framing camera image and b) the VIR image which was rotated to match the orientation of the framing camera image.

Values for parts of the inner slope of the crater were higher than the floor and the surroundings. This product is indicative of Ca/Fe carbonates if both overtones are present. The MIN2295_2480 product (figure 16e) showed relatively high values across the entire image but only half of the central region highlighted by the MIN2345_2537(figure 17e) product showed high values here. Parts of the crater slope also had values higher than the rest of the image. The product indicates the presence of Mg carbonates if both overtones are present. The products that detect carbonates all highlighted the central region where the faculae are present (figure16e,17e,18e,19e). Previous studies have shown that carbonates are present in these regions. No new regions with carbonates were detected by the summary products used in this study.

The wavelength maps for ranges 2.5-3.9 μm (figure 25) and 3.9-4.5 μm (figure 26) showed three regions from which spectra were extracted. The average spectra of these regions and pixel spectra from the center of the Occator crater can be seen in figure 34. The spectra for region A showed absorption features at 2.76 μm, 3.19 μm, ~3.5 μm and 4 μm. The average spectra for B

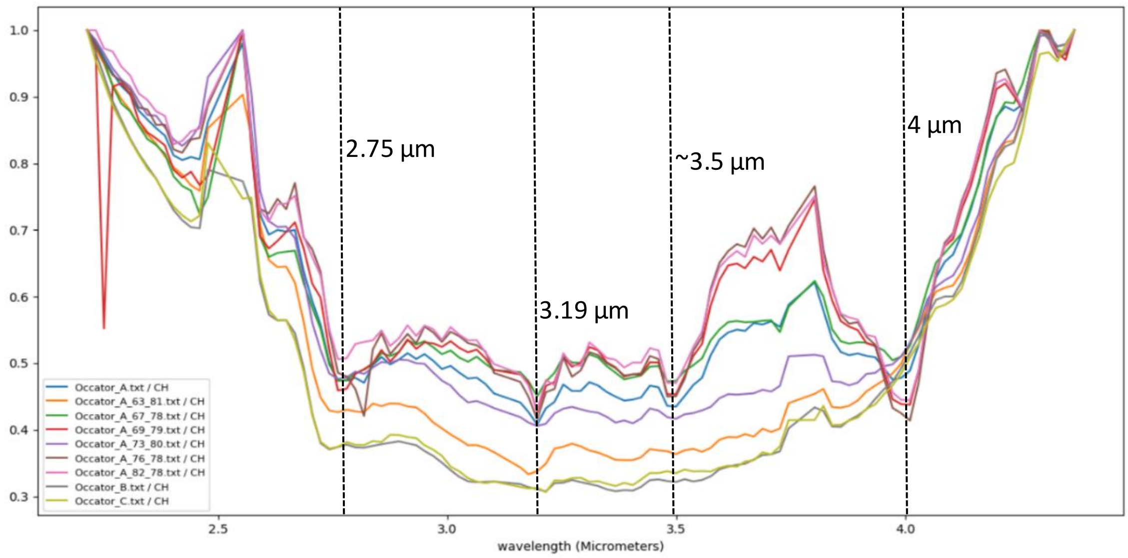

Figure 35: Average spectra of the regions identified in the wavelength maps, and pixel spectra from the center of the Occator crater

and C showed features at 2.74 μm, 3.3 μm, 3.4 μm and 3.8 μm. The study by De Sanctis et al., (2016) identified the features (figure 36) from 2.72 μm to 2.76 μm as features produced by metal hydroxide absorptions namely Mg-OH and Al-OH and attributes them to the presence of Al/Mg phyllosilicates. The paper also states that absorptions at 3.4 μm and 3.9 μm are indicative of carbonates which was distinctly seen in region A at the center of Occator crater. Pixel (69,79) at the center of region A showed an absorption feature at 2.25 μm attributed to NH_4 present in salts (De Sanctis et al., 2016). Pixel (82,78) also showed an absorption at 2.25 μm although the

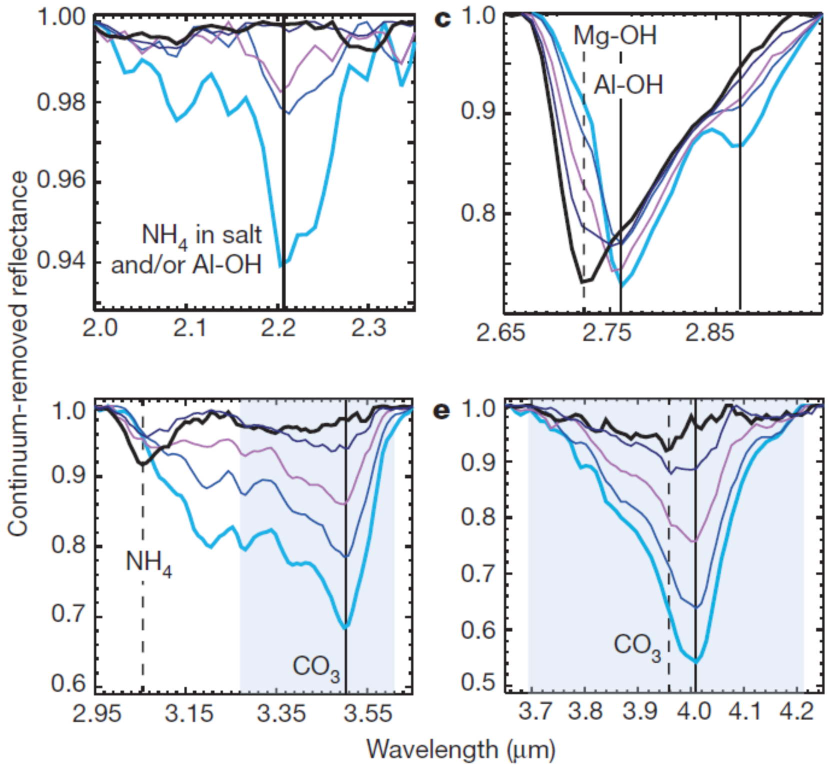

Figure 37: Spectral absorption features in the Occator spectra (De Sanctis et al., 2016). The coloured region represents anhydrous carbonate absorption regions

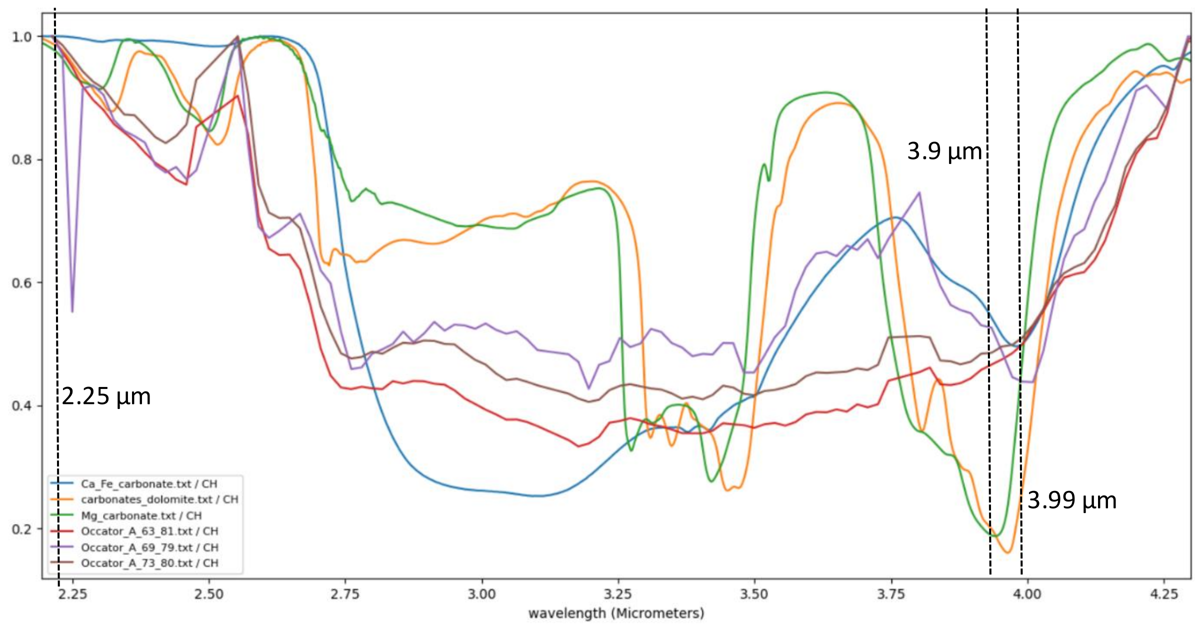

Figure 36: Spectra showing a comparison of the absorption feature positions in the RELAB spectra and the spectra from this study. Dashed lines show the absorption features for NH_4^+ salts at 2.25 µm and CO_3^{2-} at 3.99 µm. The RELAB spectra show the carbonate absorption feature at 3.9 µm.

depth was much smaller than that of pixel (69,79). Anhydrous carbonate absorption bands are also shown in figure between 3.25-3.65 μm and 3.7-4.2 μm which indicate the presence of carbonates in regions B and C.

The wavelength map showed a striated pattern outside the crater in region C which on observing the geological map of the crater (figure 38) appears to be furrows. The average spectrum of region C showed an absorption feature between 3.1-3.2 μm which I attribute to carbonates. The reason behind the presence of this feature along the furrows is unknown. It would be of interest to determine the time of formation of the deposits, and whether they were already present and merely shifted along the furrows that formed with the crater. However, this was not determined during the course of my study.

The higher values in the ice band depth products and the carbonate products along crater slopes was initially thought to be a result of the topography influencing the reflectance values since a photometric correction could not be carried out, but the spectra from region B (crater slope) and C (region surrounding the crater) show shallow absorption features at 3.35 μm and 3.85 μm which indicate anhydrous carbonate band positions (De Sanctis et al., 2016).

Two summary products showing Al-OH minerals- MIN2200 and BD2250 showed high values in the regions where the CINDEX product (that shows carbonates) showed low values and low values in the regions where CINDEX showed high values. This could indicate that that carbonate deposits cover the Al-OH minerals and these products could be used to identify regions with low Al-OH content where further studies on carbonate deposits could be carried out. These products can be seen in annex 2 but were not analysed further as the primary objective of this study was focused on brine deposits.

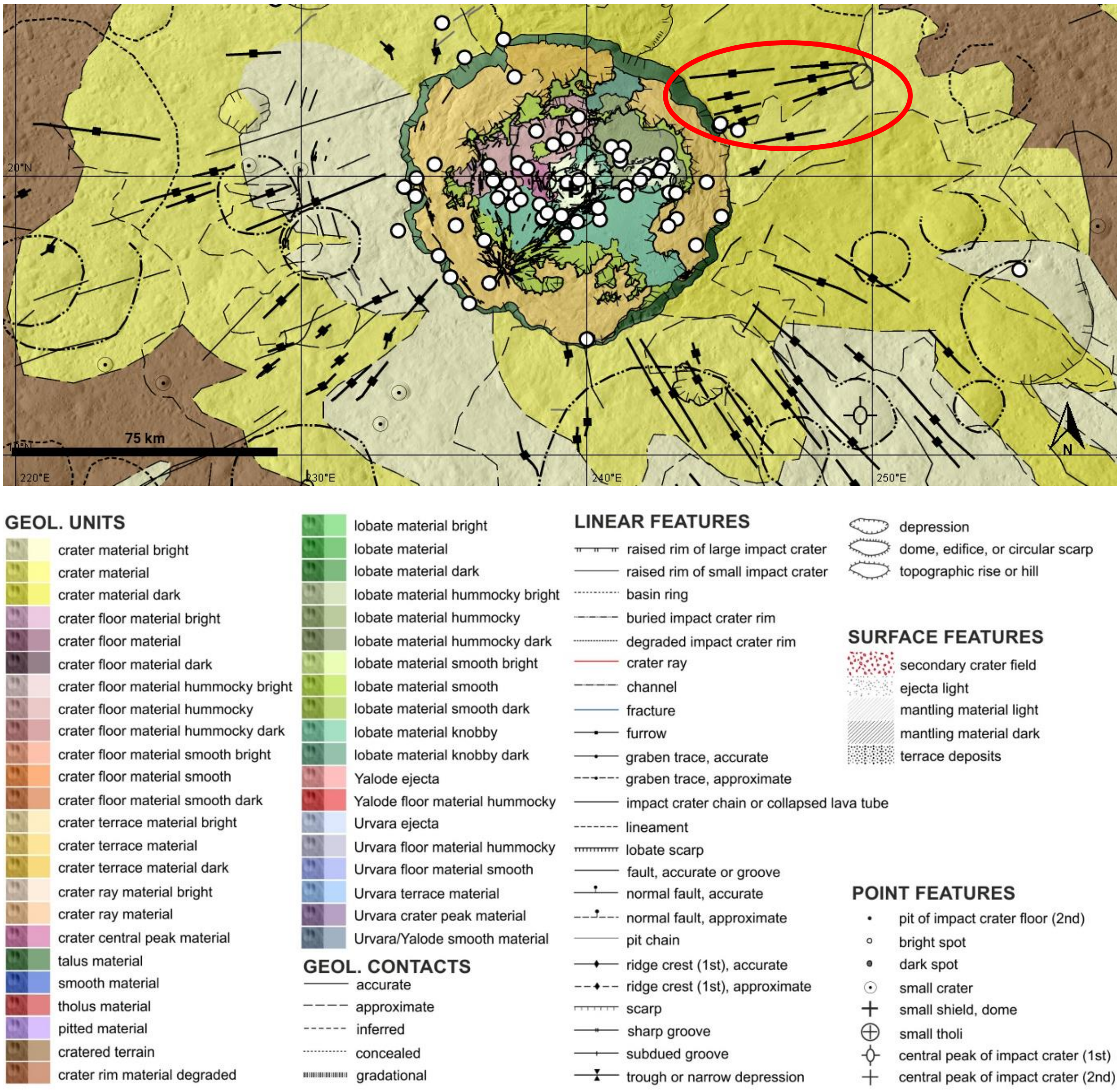

Figure 38: Geological map of the Occator crater (JMARS) showing the crater slope talus, furrows around the crater and faculae on the crater floor

4.3.2. The Haulani crater

The water ice products did not show any features as the BD1500_2 product was affected by vertical striping and the BD3100 product could not be created as one of the required bands was removed during the artifact removal stage. The ICER2 product (figure 14d) showed high values across the entire image and highlighted some parts of the inner slope of the Haulani crater and two craters beside it as having very high values. The BD2600 product (figure 13d) highlighted some of the crater slopes as well as a lot of vertical stripes in the image. This product highlights water vapour which logically should not be in the crater slopes. I believe this could imply that this product might be sensitive to some other feature of the spectrum although I could not ascertain whether this feature was due to a surface material or an error in the dataset. This result would also mean that the presence of water vapour in the Occator crater image might be incorrect.

The MIN2295_2480 and BD3400_2 showed high values across the entire image but the outlines of the Haulani crater and crater in the far-right corner of the image. The MIN2345_2537 product highlighted a lot of the striping but showed low values along the slopes of the two craters as well. The CINDEX product showed a unique result. The regions around the Haulani crater and the other craters in the image had higher values than the regions further away from them. The Haulani crater floor and the region right outside the crater had the highest values as well as the crater slopes of all the craters. This image had many craters in it but the carbonate products showed high values on the crater floor of the two largest which could indicate a relationship between the crater size and the presence of the faculae on the floor.

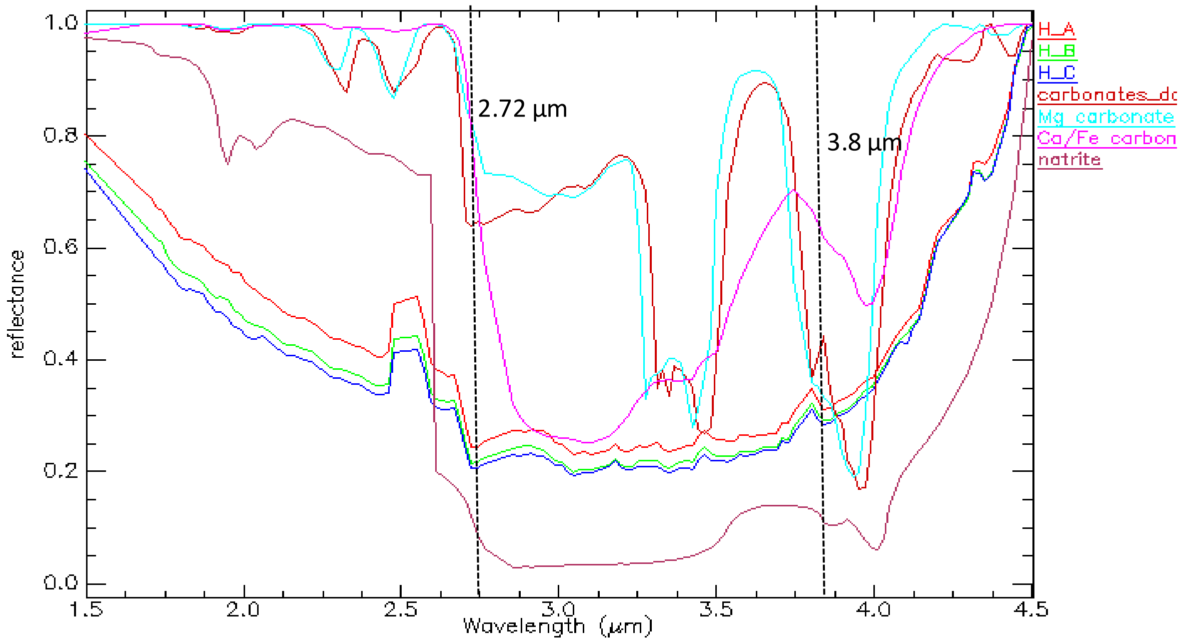

Figure 39: Haulani crater spectra compared with RELAB spectra of cabonates- Mg carbonate, Ca/Fe carbonate and natrite.

The wavelength map for 2.5-3.9 μm showed three regions of interest for Haulani crater. Region A's (crater floor) spectrum had higher reflectance values. On comparing the spectra of the three regions to the RELAB spectra, they all showed the same absorption feature at 3.85 μm that was seen in the natrite spectrum and at 2.72 μm similar to that in the carbonate spectrum (that was mostly composed of dolomite).

4.3.3. The Dantu crater

The ICER2 product (figure 14) shows moderately high values in the images but low values along the inner slope of the crater in image 14a and higher values along the crater slopes in 14b and 14c. The BD1500_2 product (figure 12) shows high values along the crater slopes in image 12a and 12c and along the crater floor and part of the surrounding regions in image 12b. The BD3100 product (figure 15) showed high values across all three images, with higher values inside the crater in image 15b and 15c and along the crater slopes in image 15b. The BD2600 product (figure 13) showed a region with high values along the crater slope in image 13c.

The MIN2345_2537 product (figure 17) highlighted the inner slope distinctly in image 17a but showed low values for the slope in image 17b and 17c however, the crater rims had high values. The MIN2295_2400 product (figure 16) showed the opposite results of MIN_2345_2537 with regions showing high values in one product showing low values in the other. Products MIN_2345_2537 and MIN2295_2400 highlight Ca/Fe carbonates and Mg carbonates respectively, and show that these carbonate minerals do not occur together although a definitive statement about this relationship can only be made by comparing spectra from these regions but the spectra did not show any differences.

The CINDEX2 (figure 19) and BD3400_2 (figure 18) products highlighted a lot of the vertical striping which can be seen in the same parts in all three images (a,b&c) and can hence be ignored. The CINDEX2 product highlighted some smaller regions with very high values both inside and outside the crater. The BD3400_2 product showed higher values along the crater slopes in image 18b and lower values along the slope in image 18a. It also highlighted regions with high values outside the crater in image 18b. These regions could be ejecta from the impact because of their random orientation and their location outside the crater.

The wavelength map for VIR_IR_1B_1_495408230_1 (figure 20a) of the Dantu crater highlighted some parts of the crater floor and regions surrounding the crater. The spectra from this image seen in figure 38 are similar but show differences in the absorption feature positions between 3-3.5 μm. The map for image VIR_IR_1B_1_495474811_1 (figure 22a) had only one deepest feature between 3.1-3.2 μm.

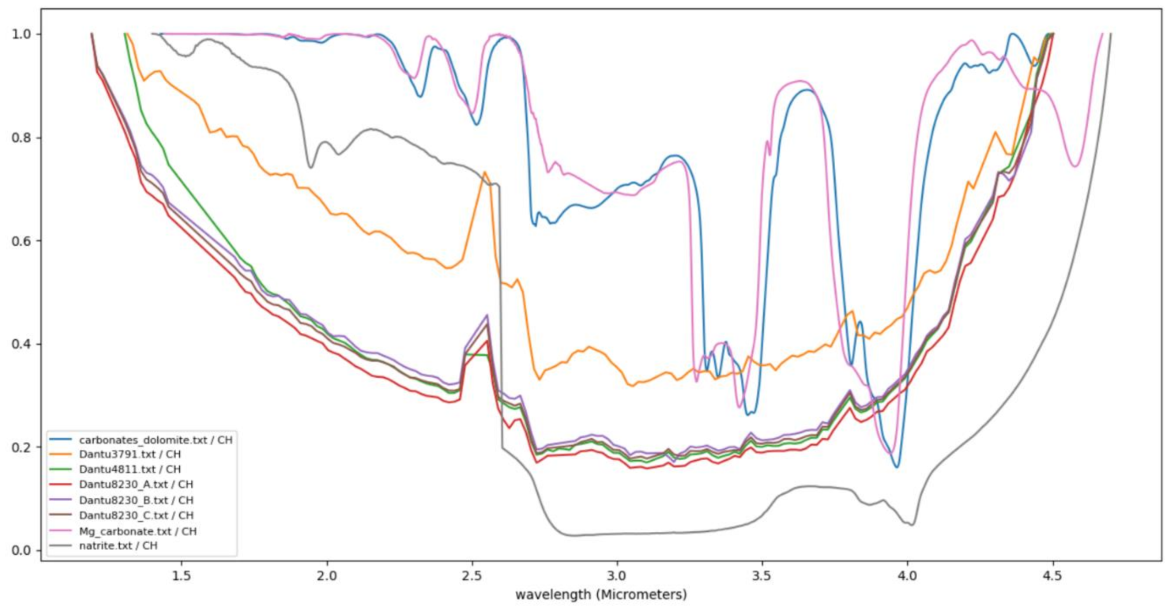

Figure 40: Dantu crater spectra compared with RELAB spectra of cabonates- Mg carbonate, Ca/Fe carbonate and natrite.

The three regions from the VIR_IR_1B_1_495408230_1 image (figure 20a) a showed similar spectrum indicating that they all were composed of the same material. They all had a shallow absorption feature at 2.72 µm similar to the carbonate (dolomite) spectrum and a feature at 3.8 µm similar to natrite. The spectrum for VIR_IR_1B_1_494523791_1 also showed a much higher reflectance than the other spectra for the crater.

4.4. Summary of the spectral analysis

The summary products highlighted the H_2O ice, CO_2 ice and carbonates but they cannot be used to quantify mineral abundance (Viviano-Beck et al., 2014) as other factors such as the size of the particles, surface albedo and mineral mixtures may affect the band depth-abundance relationship (Clark and Roush, 1984; Viviano-Beck et al., 2014).

Wavelength mapping highlighted regions of interest in the craters, and was able to give a broad mineral group like those containing CO_3 or NH_4 compounds and matched certain features in the RELAB spectra, specific minerals could not be identified because there was no perfect match with any mineral. However, the spectra did show the same features as those produced by previous studies of the faculae. The wavelength maps (figure 20-26) were also able to identify regions of interest from where the average spectra extracted showed absorption features indicative of Ca/Mg/Fe carbonates, NH_4 salts and Al-OH from all three craters. This method could therefore be used as a preliminary mapping method on other small bodies in the Solar System as well for a fast yet efficient spectral mapping.

4.5. Limitations

The biggest limitation to using the VIR datasets in this study was a tedious preprocessing process. The datasets were affected by spectral artifacts that rendered entire bands unusable.

All the code available in the PDS archive to process the data was in Interactive Data Language (IDL) which is not a very common coding language outside the remote sensing community specially to process hyperspectral cubes, and finding repositories to fix any bugs was harder than I anticipated. As a researcher with a basic knowledge of Python and Matlab, learning IDL just for a few preprocessing steps seemed futile. I did create a python code to convert .LBL file information to ENVI header files and will make this available in the ITC data archive.

During this study I came across ISIS, a tool designed by USGS specifically to process and manipulate data from space missions, however ISIS only runs on Linux and the steps to download it were not easy to follow for someone not used to the terminology used especially because of two very important path variables that point to where the software files are stored. I was able to find a blog written a few years ago[4] that explained the process in a much simpler manner and helped me download a missing folder after which I was finally able to run ISIS3. Newer releases exist but I wasn't able to correctly download the software and the datasets required for those versions to be able to run them.

While ISIS has tools to carry out radiometric corrections and elaborate destriping procedures for other missions like the Mars Reconnaissance Orbiter (MRO), only two mission specific tools were available for the Dawn mission- dawnvir2isis and dawnfc2isis which convert files from PDS cubes/images to ISIS cubes. An ISIS cube can only be exported as a .IMG file. ISIS cubes can be opened in QGIS but not in ENVI or HypPy.

The map projection in ISIS used a DTM that did not match with the one used in JMARS Ceres or the surface maps available on the PDS archive which made it impossible to display all the datasets together.

[4] willyingling.com/research-blog/2019/5/9/how-to-installing-isis3-on-a-windows-computer

5. CONCLUSIONS AND RECOMMENDATIONS

This section shows the conclusions made during this study and provides recommendations on how this research can help future studies.

5.1. Conclusions

The VIR datasets contained a lot of spectral artifacts mainly due to sensor defects, like negative pixels, spikes and vertical stripes that affected all wavelengths. This study anticipated the data to have artifacts but the extent to which the artifacts affected the data turned out to be a major hinderance. Even after the artifact removal procedure some striping still persisted and was visible in the summary products and wavelength maps. These artifacts made interpreting the maps difficult as it involved looking past the artifacts at the surface features seen in the maps. Conventional preprocessing steps like solar correction were be applied but a drawback of this study was the inability to carry out a photometric correction and map project the datasets before spectral analysis. The datasets were later map projected in ISIS and seemed to be stretched to a great extent.

The preprocessing methods used in this study did not use the artifact matrix created by the VIR instrument team due to issues with the code. The artifact removal process used in place of the matrix was able to sufficiently suppress the spectral artifacts like spikes and negative pixels and reduce vertical stripes, while not destroying any spectral signatures. The spectra obtained after the artifact removal were comparable to those produced by previous studies that used the artifact matrix.

The summary products for H_2O ice, CO_2 ice and carbonates showed regions of high and low values along the crater slopes, crater floor and surrounding regions. The product for water vapour also highlighted the region in the center of the crater where faculae are known to occur. The regions highlighted were the same as the ones in the wavelength maps.

The wavelength maps identified regions from where spectra were collected. These spectra showed absorption features indicative of Ca/Mg/Fe carbonates, AlOH and NH_4 salts in all three craters, however it should be noted that the spectra obtained by me could only be compared to one feature in each of the RELAB spectra and while the carbonate or phyllosilicate group might be present, the specific minerals of that group cannot be inferred with certainty. The wavelength maps also highlighted deposits along furrows in the regions surrounding Occator crater and along its crater talus slopes.

All of the minerals and spectral absorption features identified from the maps or summary products in this study were already identified in previous studies, and no new minerals were discovered within the craters. The three craters show the presence of the same minerals however the reflectance values of the Occator crater floor faculae were higher than the rest.

This study's purpose was to investigate brine pockets on Ceres. It aimed to use a method that analysed the spectra of the entire datacube in search of spectral features, highlighting these regions and determining what chemical constituents produced these features. It was not able to identify any minerals with certainty as the spectra I obtained only matched parts of the spectra for minerals from the RELAB database. Due to this I was not able to study the relations between faculae minerals and possible implications this could have on the subsurface pockets.

5.2. Recommendations

Future studies on the surface mineralogy of Ceres using hyperspectral imagery should keep in mind that the artifact removal procedure is tedious and time consuming and the workplan for the study should have to be modified according to this. I would also recommend downloading and learning how to operate ISIS when dealing with extra-terrestrial datasets as it was made for this purpose and has many more tools for older missions like the Mars Reconnaissance Orbiter and Cassini.

Future studies could focus on the thermal infrared region of the spectrum. The summary products in this region did highlight features, however I had not anticipated using this region and had not carried out a thermal correction and removed the bands in the subsetting stage. This region does however have more vertical stripes and may need an improved artifact removal procedure.

The Dawn spacecraft visited asteroid Vesta before Ceres due to an increased interest in the asteroid belt and its role in understanding the early Solar System. A comparison of the two bodies using summary products as a starting point can be carried out as well as a discussion on the differences between them and what caused this.

LIST OF REFERENCES

Baldridge, A.M., Hook, S.J., Crowley, J.K., Marion, G.M., Kargel, J.S., Michalski, J.L., Thomson, B.J., De Souza Filho, C.R., Bridges, N.T., Brown, A.J., 2009. Contemporaneous deposition of phyllosilicates and sulfates: Using Australian acidic saline lake deposits to describe geochemical variability on Mars. Geophys. Res. Lett. 36, 19201. https://doi.org/10.1029/2009GL040069

Barducci, A., Pippi, I., 2001. Analysis and rejection of systematic disturbances in hyperspectral remotely sensed images of the Earth. Appl. Opt. 40, 1464. https://doi.org/10.1364/ao.40.001464

Bland, M.T., Raymond, C.A., Schenk, P.M., Fu, R.R., Kneissl, T., Pasckert, J.H., Hiesinger, H., Preusker, F., Park, R.S., Marchi, S., King, S.D., Castillo-Rogez, J.C., Russell, C.T., 2016. Composition and structure of the shallow subsurface of Ceres revealed by crater morphology. Nat. Geosci. 9, 538–542. https://doi.org/10.1038/ngeo2743

Bowling, T.J., Ciesla, F.J., Davison, T.M., Scully, J.E.C., Castillo-Rogez, J.C., Marchi, S., Johnson, B.C., 2019. Post-impact thermal structure and cooling timescales of Occator crater on asteroid 1 Ceres. Icarus 320, 110–118. https://doi.org/10.1016/j.icarus.2018.08.028

Carrozzo, F.G., Raponi, A., De Sanctis, M.C., Ammannito, E., Giardino, M., D’Aversa, E., Fonte, S., Tosi, F., 2016. Artifacts reduction in VIR/Dawn data. Rev. Sci. Instrum. 87. https://doi.org/10.1063/1.4972256

Carry, B., Dumas, C., Fulchignoni, M., Merline, W.J., Berthier, J., Hestroffer, D., Fusco, T., Tamblyn, P., 2008. Near-infrared mapping and physical properties of the dwarf-planet Ceres. Astron. Astrophys. 478, 235–244. https://doi.org/10.1051/0004-6361:20078166

Castillo-Rogez, J., Scully, J., Neveu, M., Wyrick, D., Thangjam, G., Rivkin, A., Sori, M., Vinogradoff, V., Miller, K., Ermakov, A., Hughson, K., Quick, L., Nathues, A., Sanctis, M.C. De, 2021. Science Motivations for the Future Exploration of Ceres. Bull. AAS 53. https://doi.org/10.3847/25c2cfeb.542c3be2

Clark, R.N., Roush, T.L., 1984. Reflectance spectroscopy: quantitative analysis techniques for remote sensing applications. J. Geophys. Res. 89, 6329–6340. https://doi.org/10.1029/JB089iB07p06329

De Sanctis, M.C., Ammannito, E., Raponi, A., Frigeri, A., Ferrari, M., Carrozzo, F.G., Ciarniello, M., Formisano, M., Rousseau, B., Tosi, F., Zambon, F., Raymond, C.A., Russell, C.T., 2020. Fresh emplacement of hydrated sodium chloride on Ceres from ascending salty fluids. Nat. Astron. 4, 786–793. https://doi.org/10.1038/s41550-020-1138-8

De Sanctis, M.C., Ammannito, E., Raponi, A., Marchi, S., McCord, T.B., McSween, H.Y., Capaccioni, F., Capria, M.T., Carrozzo, F.G., Ciarniello, M., Longobardo, A., Tosi, F., Fonte, S., Formisano, M., Frigeri, A., Giardino, M., Magni, G., Palomba, E., Turrini, D., Zambon, F., Combe, J.P., Feldman, W., Jaumann, R., McFadden, L.A., Pieters, C.M., Prettyman, T., Toplis, M., Raymond, C.A., Russell, C.T., 2015. Ammoniated phyllosilicates with a likely outer Solar System origin on (1) Ceres. Nature 528, 241–244. https://doi.org/10.1038/nature16172

De Sanctis, M.C., Coradini, A., Ammannito, E., Filacchione, G., Capria, M.T., Fonte, S., Magni, G., Barbis, A., Bini, A., Dami, M., Ficai-Veltroni, I., Preti, G., 2012. The VIR spectrometer, in: The Dawn Mission to Minor Planets 4 Vesta and 1 Ceres. Springer, New York, NY, pp. 329–369. https://doi.org/10.1007/978-1-4614-4903-4_13

De Sanctis, M.C., Raponi, A., Ammannito, E., Ciarniello, M., Toplis, M.J., McSween, H.Y., Castillo-Rogez, J.C., Ehlmann, B.L., Carrozzo, F.G., Marchi, S., Tosi, F., Zambon, F., Capaccioni, F., Capria, M.T., Fonte, S., Formisano, M., Frigeri, A., Giardino, M., Longobardo, A., Magni, G., Palomba, E., McFadden, L.A., Pieters, C.M., Jaumann, R., Schenk, P., Mugnuolo, R., Raymond, C.A., Russell, C.T., 2016. Bright carbonate deposits as evidence of aqueous alteration on (1) Ceres. Nature 536, 54–57. https://doi.org/10.1038/nature18290

De Sanctis, M.C., Vinogradoff, V., Raponi, A., Ammannito, E., Ciarniello, M., Carrozzo, F.G., De Angelis, S., Raymond, C.A., Russell, C.T., 2019. Characteristics of organic matter on Ceres from VIR/Dawn high spatial resolution spectra. Mon. Not. R. Astron. Soc. 482, 2407–2421. https://doi.org/10.1093/mnras/sty2772

Gómez-Chova, L., Alonso, L., Guanter, L., Gustavo, C.V., Calpe, J., Moreno, J., 2008. Correction of systematic spatial noise in push-broom hyperspectral sensors: Application to CHRIS/PROBA images. Appl. Opt. 47, F46–F60. https://doi.org/10.1364/AO.47.000F46

Greeley, R., Batson, R., 1990. Planetary mapping.

Küppers, M., O’Rourke, L., Bockelée-Morvan, D., Zakharov, V., Lee, S., Von Allmen, P., Carry, B.,

Teyssier, D., Marston, A., Müller, T., Crovisier, J., Barucci, M.A., Moreno, R., 2014. Localized sources of water vapour on the dwarf planet (1) Ceres. Nature 505, 525–527. https://doi.org/10.1038/nature12918
Manga, M., Wang, C.Y., 2007. Pressurized oceans and the eruption of liquid water on Europa and Enceladus. Geophys. Res. Lett. 34. https://doi.org/10.1029/2007GL029297
Marchi, S., Ermakov, A.I., Raymond, C.A., Fu, R.R., O'Brien, D.P., Bland, M.T., Ammannito, E., De Sanctis, M.C., Bowling, T., Schenk, P., Scully, J.E.C., Buczkowski, D.L., Williams, D.A., Hiesinger, H., Russell, C.T., 2016. The missing large impact craters on Ceres. Nat. Commun. 7. https://doi.org/10.1038/ncomms12257
Martin, C.R., Binzel, R.P., 2021. Ammonia-water freezing as a mechanism for recent cryovolcanism on Pluto. Icarus 356, 113763. https://doi.org/10.1016/j.icarus.2020.113763
McCord, T.B., Combe, J.-P., Castillo-Rogez, J.C., McSween, H.Y., Prettyman, T.H., 2021. Ceres, a wet planet: The view after Dawn. Geochemistry 125745. https://doi.org/10.1016/J.CHEMER.2021.125745
Mest, S.C., Neesemann, A., Crown, D.A., Berman, D.C., Pasckert, J.H., Schmedemann, N., Marchi, S., Hiesinger, H., Buczkowski, D.L., Scully, J.E.C., Williams, D.A., Yingst, R.A., Platz, T., Jaumann, R., Roatsch, T., Preusker, F., Nathues, A., Raymond, C.A., Russell, C.T., 2021. The Chronostratigraphy of Ceres. Lunar Planet. Sci. Conf. 2055, 2055.
Moroz, L. V, Arnold, G., Korochantsev, A. V, Wäsch, R., 1998. Natural Solid Bitumens as Possible Analogs for Cometary and Asteroid Organics:: 1. Reflectance Spectroscopy of Pure Bitumens. Icarus 134, 253–268. https://doi.org/10.1006/icar.1998.5955
Nathues, A., Hoffmann, M., Schaefer, M., Le Corre, L., Reddy, V., Platz, T., Cloutis, E.A., Christensen, U., Kneissl, T., Li, J.Y., Mengel, K., Schmedemann, N., Schaefer, T., Russell, C.T., Applin, D.M., Buczkowski, D.L., Izawa, M.R.M., Keller, H.U., O'Brien, D.P., Pieters, C.M., Raymond, C.A., Ripken, J., Schenk, P.M., Schmidt, B.E., Sierks, H., Sykes, M. V., Thangjam, G.S., Vincent, J.B., 2015. Sublimation in bright spots on (1) Ceres. Nature 528, 237–240. https://doi.org/10.1038/nature15754
Park, R.S., Konopliv, A.S., Bills, B.G., Rambaux, N., Castillo-Rogez, J.C., Raymond, C.A., Vaughan, A.T., Ermakov, A.I., Zuber, M.T., Fu, R.R., Toplis, M.J., Russell, C.T., Nathues, A., Preusker, F., 2016. A partially differentiated interior for (1) Ceres deduced from its gravity field and shape. Nature 537, 515–517. https://doi.org/10.1038/nature18955
Pieters, C.M., 1983. STRENGTH OF MINERAL ABSORPTION FEATURES IN THE TRANSMITTED COMPONENT OF NEAR-INFRARED REFLECTED LIGHT: FIRST RESULTS FROM RELAB. J. Geophys. Res. 88, 9534–9544. https://doi.org/10.1029/JB088iB11p09534
Pilcher, F., 1989. The circumstances of minor planet discovery, in: Asteroids II. pp. 1002–1033.
Raponi, A., Carrozzo, F.G., Zambon, F., De Sanctis, M.C., Ciarniello, M., Frigeri, A., Ammannito, E., Tosi, F., Combe, J.P., Longobardo, A., Palomba, E., Pieters, C.M., Raymond, C.A., Russell, C.T., 2019. Mineralogical mapping of Coniraya quadrangle of the dwarf planet Ceres. Icarus 318, 99–110. https://doi.org/10.1016/j.icarus.2017.10.023
Raymond, C. A., Roatsch, T., 2015. Ceres coordinate system description [WWW Document].
Rousseau, B., Raponi, A., Ciarniello, M., Ammannito, E., Carrozzo, F.G., De Sanctis, M.C., Fonte, S., Frigeri, A., Tosi, F., 2019. Correction of the VIR-visible data set from the Dawn mission. Rev. Sci. Instrum. 90, 123110. https://doi.org/10.1063/1.5123362
Ruesch, O., Quick, L.C., Landis, M.E., Sori, M.M., Čadek, O., Brož, P., Otto, K.A., Bland, M.T., Byrne, S., Castillo-Rogez, J.C., Hiesinger, H., Jaumann, R., Krohn, K., McFadden, L.A., Nathues, A., Neesemann, A., Preusker, F., Roatsch, T., Schenk, P.M., Scully, J.E.C., Sykes, M. V., Williams, D.A., Raymond, C.A., Russell, C.T., 2019. Bright carbonate surfaces on Ceres as remnants of salt-rich water fountains. Icarus 320, 39–48. https://doi.org/10.1016/j.icarus.2018.01.022
Russell, C.T., Raymond, C.A., Ammannito, E., Buczkowski, D.L., De Sanctis, M.C., Hiesinger, H., Jaumann, R., Konopliv, A.S., McSween, H.Y., Nathues, A., Park, R.S., Pieters, C.M., Prettyman, T.H., McCord, T.B., McFadden, L.A., Mottola, S., Zuber, M.T., Joy, S.P., Polanskey, C., Rayman, M.D., Castillo-Rogez, J.C., Chi, P.J., Combe, J.P., Ermakov, A., Fu, R.R., Hoffmann, M., Jia, Y.D., King, S.D., Lawrence, D.J., Li, J.Y., Marchi, S., Preusker, F., Roatsch, T., Ruesch, O., Schenk, P., Villarreal, M.N., Yamashita, N., 2016. Dawn arrives at ceres: Exploration of a small, volatile-rich world. Science (80-.). 353, 1008–1010.

https://doi.org/10.1126/science.aaf4219
Scully, J.E.C., Schenk, P.M., Castillo-Rogez, J.C., Buczkowski, D.L., Williams, D.A., Pasckert, J.H., Duarte, K.D., Romero, V.N., Quick, L.C., Sori, M.M., Landis, M.E., Raymond, C.A., Neesemann, A., Schmidt, B.E., Sizemore, H.G., Russell, C.T., 2020. The varied sources of faculae-forming brines in Ceres' Occator crater emplaced via hydrothermal brine effusion. Nat. Commun. 11. https://doi.org/10.1038/S41467-020-15973-8
Sides, S.C., Becker, T.L., Becker, K.J., Edmundson, K.L., Backer, J.W., Wilson, T.J., Weller, L.A., Humphrey, I.R., Berry, K.L., Shepherd, M.R., Hahn, M.A., Rose, C.C., Rodriguez, K., Paquette, A.S., Mapel, J.A., Shinaman, J.R., Richie, J.O., 2017. The USGS Integrated Software for Imagers and Spectrometers (ISIS 3) Instrument Support, New Capabilities, and Releases. 48th Lunar Planet. Sci. Conf.
Sierks, H., Keller, H.U., Jaumann, R., Michalik, H., Behnke, T., Bubenhagen, F., Büttner, I., Carsenty, U., Christensen, U., Enge, R., Fiethe, B., Gutiérrez Marqués, P., Hartwig, H., Krüger, H., Kühne, W., Maue, T., Mottola, S., Nathues, A., Reiche, K.U., Richards, M.L., Roatsch, T., Schröder, S.E., Szemerey, I., Tschentscher, M., 2011. The Dawn framing camera. Space Sci. Rev. 163, 263–327. https://doi.org/10.1007/s11214-011-9745-4
Stein, N.T., Ehlmann, B.L., Palomba, E., De Sanctis, M.C., Nathues, A., Hiesinger, H., Ammannito, E., Raymond, C.A., Jaumann, R., Longobardo, A., Russell, C.T., 2019. The formation and evolution of bright spots on Ceres. Icarus 320, 188–201. https://doi.org/10.1016/j.icarus.2017.10.014
Thomas, P.C., Parker, J.W., McFadden, L.A., Russell, C.T., Stern, S.A., Sykes, M. V., Young, E.F., 2005. Differentiation of the asteroid Ceres as revealed by its shape. Nature 437, 224–226. https://doi.org/10.1038/nature03938
Van Ruitenbeek, F.J.A., Bakker, W.H., Van Der Werff, H.M.A., Zegers, T.E., Oosthoek, J.H.P., Omer, Z.A., Marsh, S.H., Van Der Meer, F.D., 2014. Mapping the wavelength position of deepest absorption features to explore mineral diversity in hyperspectral images. Planet. Space Sci. 101, 108–117. https://doi.org/10.1016/j.pss.2014.06.009
Viviano-Beck, C.E., Seelos, F.P., Murchie, S.L., Kahn, E.G., Seelos, K.D., Taylor, H.W., Taylor, K., Ehlmann, B.L., Wisemann, S.M., Mustard, J.F., Morgan, M.F., 2014. Revised CRISM spectral parameters and summary products based on the currently detected mineral diversity on Mars. J. Geophys. Res. Planets 119, 1403–1431. https://doi.org/10.1002/2014JE004627
Williams, D.A., Buczkowski, D.L., Mest, S.C., Scully, J.E.C., Platz, T., Kneissl, T., 2018. Introduction: The geologic mapping of Ceres. Icarus 316, 1–13. https://doi.org/10.1016/j.icarus.2017.05.004

APPENDIX

Annex 1: Ground correction factor

S1*Spectrum(S1.w,[0.898316, 0.890987, 0.882893, 0.874227, 0.865063, 0.858167, 0.852843, 0.849373, 0.846218, 0.843248, 0.840359, 0.837533, 0.834886, 0.832317, 0.828994, 0.826036, 0.823337, 0.820822, 0.818445, 0.816170, 0.813982, 0.811874, 0.809853, 0.807939, 0.806144, 0.804465, 0.802900, 0.801425, 0.800004, 0.798619, 0.797251, 0.795889, 0.794531, 0.793184, 0.791848, 0.790534, 0.789230, 0.787912, 0.786550, 0.785122, 0.783618, 0.782031, 0.780342, 0.778531, 0.776582, 0.774499, 0.772302 , 0.769993, 0.767589, 0.765117, 0.762582, 0.759974, 0.757279, 0.754471, 0.751539, 0.748480, 0.745292, 0.741996, 0.738631, 0.735233, 0.731830, 0.728450, 0.725112, 0.721850, 0.718695, 0.715657, 0.712742, 0.709959, 0.707321, 0.704848, 0.702549, 0.700428, 0.698492, 0.696754, 0.695216, 0.693865, 0.692676, 0.691630, 0.690719, 0.689930, 0.689249, 0.688674, 0.688203, 0.687826, 0.687518, 0.687259, 0.687040, 0.686836, 0.686621, 0.686389, 0.686128, 0.685840, 0.685527, 0.685189, 0.684824, 0.684443, 0.684058, 0.683685, 0.683334, 0.683011, 0.682726, 0.682493, 0.682311, 0.682174, 0.682079, 0.682023, 0.682001, 0.682010, 0.682058, 0.682149, 0.682276, 0.682432, 0.682612, 0.682809, 0.683023, 0.683252, 0.683487, 0.683731, 0.683982, 0.684235, 0.684479, 0.684700, 0.684881, 0.685015, 0.685095, 0.685117, 0.685082, 0.684992, 0.684850, 0.684655, 0.684408, 0.684110, 0.683767, 0.683387, 0.682979, 0.682550, 0.682110, 0.681665, 0.681220, 0.680783, 0.680354, 0.679940, 0.679544, 0.679173, 0.678828, 0.678511, 0.678222, 0.677960, 0.677728, 0.677524, 0.677349, 0.677205, 0.677091, 0.677008, 0.676952, 0.676917, 0.676897, 0.676887, 0.676885])

Annex 2: Summary products showing Al-OH minerals

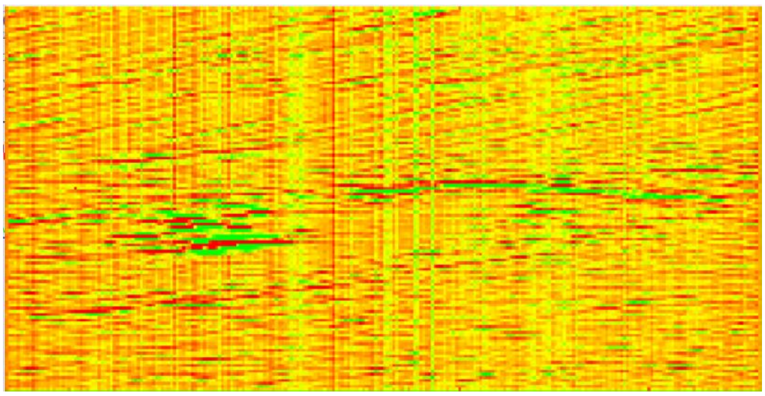

BD2250

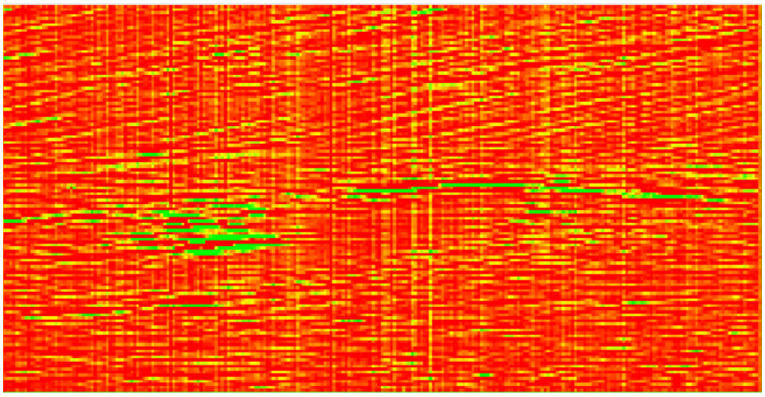

MIN2200

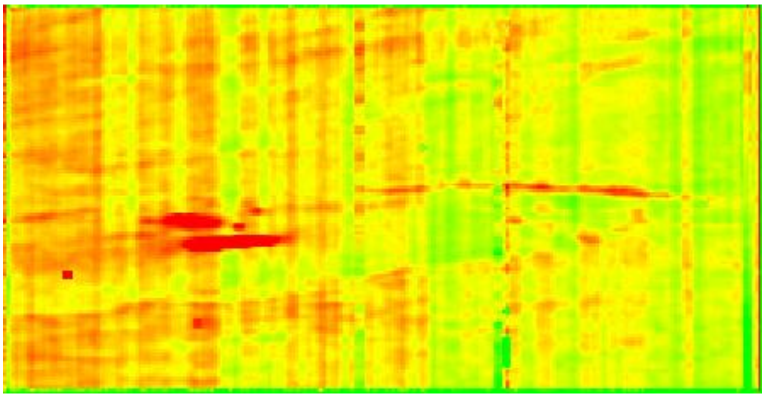

CINDEX

Summary products showing Al-OH minerals- MIN2200 and BD2250 showed low values in the regions where the CINDEX product (that shows carbonates) showed high values ie. along the crater slope and in the center of the crater.